Estimates of Surface Waves Using Subsurface EM-APEX Floats under Typhoon Fanapi 2010

JE-YUAN HSU, REN-CHIEH LIEN, ERIC A. D'ASARO, AND THOMAS B. SANFORD

Applied Physics Laboratory, and School of Oceanography, University of Washington, Seattle, Washington

(Manuscript received 10 July 2017, in final form 14 November 2017)

ABSTRACT

Seven subsurface Electromagnetic Autonomous Profiling Explorer (EM-APEX) floats measured the voltage induced by the motional induction of seawater under Typhoon Fanapi in 2010. Measurements were processed to estimate high-frequency oceanic velocity variance $\widetilde{\sigma_u}^2(z)$ associated with surface waves. Surface wave peak frequency f_p and significant wave height H_s are estimated by a nonlinear least squares fitting to $\widetilde{\sigma_u}^2$, assuming a broadband JONSWAP surface wave spectrum. The H_s is further corrected for the effects of float rotation, Earth's geomagnetic field inclination, and surface wave propagation direction. The f_p is 0.08–0.10 Hz, with the maximum f_p of 0.10 Hz in the rear-left quadrant of Fanapi, which is ~0.02 Hz higher than in the rear-right quadrant. The H_s is 6–12 m, with the maximum in the rear sector of Fanapi. Comparing the estimated f_p and H_s with those assuming a single dominant surface wave yields differences of more than 0.02 Hz and 4 m, respectively. The surface waves under Fanapi simulated in the WAVEWATCH III (ww3) model are used to assess and compare to float estimates. Differences in the surface wave spectra of JONSWAP and ww3 yield uncertainties of <5% outside Fanapi's eyewall and >10% within the eyewall. The estimated f_p is 10% less than the simulated f_p^{ww3} before the passage of Fanapi's eye and 20% less after eye passage. Most differences between H_s and simulated H_s^{ww3} are <2 m except those in the rear-left quadrant of Fanapi, which are ~5 m. Surface wave estimates are important for guiding future model studies of tropical cyclone wave–ocean interactions.

1. Introduction

Surface waves carried by the storm surges of tropical cyclones are disasters for coastlines. Surface waves also change the roughness of the ocean, altering the surface wind stress under tropical cyclones (Moon et al. 2004; Chen et al. 2013). The wave-dependent surface wind stress extracts the tropical cyclone's momentum to force ocean current (Emanuel 1995). The induced ocean current then leads to shear instability, vertical mixing, and cooling in the upper ocean (Price et al. 1994), thereby lessening the heat available for cyclone intensification (Lin et al. 2013). Measuring surface waves under tropical cyclones is critical for improving the parameterizations of surface wind stress in the forecast of tropical cyclone intensification (Fan et al. 2009).

The most often used platforms for measuring surface waves include wave sensors mounted on drifting buoys (e.g., Herbers et al. 2012), sensors mounted on buoys connected to moorings (e.g., Mitsuyasu et al. 1975; Steele et al. 1992; Young 1998; Graber et al. 2000; Dietrich et al. 2011; Drennan et al. 2014), satellite altimeters [e.g., *Environmental Satellite-1* (*Envisat-1*) and *European Remote-Sensing Satellite-2* (*ERS-2*) in Fan et al. 2009; Young and Burchell 1996; Young and Vinoth 2013], radar altimeters mounted on aircraft or ships (e.g., Hwang et al. 2000; Wright et al. 2001; Black et al. 2007; Magnusson and Donelan 2013), and Doppler sonar radar mounted on towers in shallow water or on coastlines (e.g., Pinkel and Smith 1987; Reichert et al. 1999; Lin et al. 2002). Deploying buoys to measure surface waves after tropical cyclones have formed is risky, when possible (Collins et al. 2014). Most tropical cyclones do not pass buoys deployed in the open ocean. Recently, however, moored buoy measurements were taken as Typhoon Nepartak's eye passed (Jan et al. 2017). Wave sensors and wire cables mounted on buoys may be damaged by strong tropical

Denotes content that is immediately available upon publication as open access.

Supplemental information related to this paper is available at the Journals Online website: https://doi.org/10.1175/JTECH-D-17-0121.s1.

Corresponding author: Je-Yuan Hsu, jyhsu@uw.edu

DOI: 10.1175/JTECH-D-17-0121.1

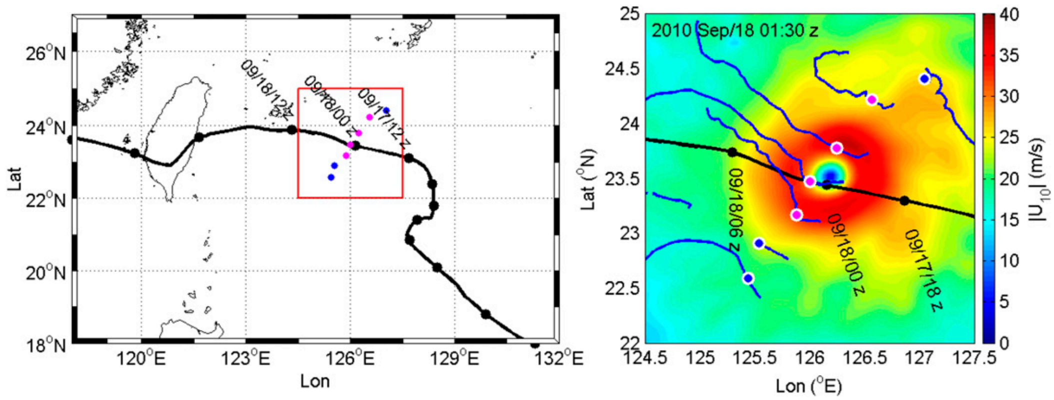

FIG. 1. (left) Typhoon Fanapi's track in the western Pacific (black curve with dots) and deployment positions of EM-APEX floats (blue and magenta dots). (right) The map of $|\mathbf{U}_{10}|$ (color shading) and EM-APEX float positions (blue and magenta dots) at 0130 UTC 18 Sep 2010 when Typhoon Fanapi arrived at the float array. Float trajectories are indicated (blue lines). Typhoon track (black line with dots) is labeled with time as month/day/hour UTC. Construction of Fanapi's wind map $|\mathbf{U}_{10}|$ is described in appendix E. The measurements taken by four EM-APEX floats (magenta dots) within 100 km of Fanapi's track are mostly at $|\mathbf{U}_{10}| > 20\,\mathrm{m\,s^{-1}}$ and are used to estimate surface wave properties in Fig. 4.

cyclone winds (e.g., $>25\,\mathrm{m\,s^{-1}}$) and turbulence at the sea surface (Collins et al. 2014). Scanning radar altimeters (SRA) mounted on aircraft have been used to study surface waves under tropical cyclones by remote sensing of ocean surface displacements (e.g., Wright et al. 2001; Black et al. 2007; Fan et al. 2009). Unfortunately, SRA backscattered signals are vulnerable to contamination by sea foam, spray, and bubbles (Magnusson and Donelan 2013), which are ubiquitous in strong tropical cyclone wind environments (Black et al. 2007).

When seawater is moved by ocean currents and surface gravity waves through Earth's geomagnetic field, an electric field is induced (Longuet-Higgins et al. 1954; Weaver 1965; Sanford 1971; Podney 1975), producing electric current in the ocean (Cox et al. 1978). The temporal variations of wave-induced electric current in the ocean will further generate an electromagnetic field according to Ampere's law (Watermann and Magunia 1997; Lilley et al. 2004). Sanford et al. (2011) measured the high-frequency velocity variance associated with the motional induction of surface waves using Electromagnetic Autonomous Profiling Explorer (EM-APEX) floats under Hurricane Frances 2004. These subsurface floats were air launched (e.g., Sanford et al. 2011; Hsu et al. 2017) from a C-130 aircraft about 1 day before the passage of the tropical cyclone's eye, and they took measurements of temperature, salinity, current velocity, and velocity variance under strong tropical cyclone winds (e.g., $>25\,\mathrm{m\,s^{-1}}$). They estimated significant wave height and the mean wave period, assuming a single dominant surface wave under the hurricane. This study aims to provide an improved method for estimating surface waves using EM-APEX float measurements by assuming a broadband surface wave spectrum. Uncertainties in the surface wave estimates are assessed.

Seven EM-APEX floats were launched from a C-130 aircraft (Mrvaljevic et al. 2013; Fig. 1) starting at 0100 UTC 17 September 2010 in Typhoon Fanapi along 126.1°E between 22.6° and 24.4°N, with a horizontal separation of ~25 km. Details of measurements taken under Typhoon Fanapi during the Impact of Typhoons on the Ocean in the Pacific (ITOP) project are described in D'Asaro et al. (2014). Section 2 describes EM-APEX float measurements. Section 3 discusses the theory of motional induction by surface wave velocity and ocean currents. Section 4 presents methods to estimate the surface wave velocity variance from float measurements and surface wave properties at the float positions assuming the empirical JONSWAP spectrum (Hasselmann et al. 1973; appendix D, section a). In section 5 we estimate surface waves under Fanapi using two methods—one assuming the JONSWAP spectrum and one assuming a single dominant surface wave (Sanford et al. 2011). The oceanic surface wave model WAVEWATCH III (ww3) is used to simulate the surface wave field under Typhoon Fanapi. In section 5 the ww3 model outputs are compared with the float estimates of surface waves. In section 7 we describe using the model study uncertainties in our surface wave estimates. Section 8 will summarize the methodology and results.

2. EM-APEX float measurements

EM-APEX floats measure temperature, salinity, and pressure between the ocean surface and 250-m depth using a Sea-Bird Electronics SBE-41 CTD sensor mounted on top of the floats. The CTD sampling rate varies from 0.025 to 0.05 Hz. The floats profile vertically by adjusting the buoyancy relative to the surrounding seawater. The average vertical profiling speed of the

TABLE 1. Notations in this study.

Notations in the equations of motional induction	
$\mathbf{J}$	Electric current
x, y, and z	Directions (positive x toward geomagnetic east, positive y toward geomagnetic north, and the depth z positive vertically upward from seafloor); x, y, and z in the subscript of the parameters represent the components in the corresponding directions
$\hat{\mathbf{i}}$, $\hat{\mathbf{j}}$, and $\hat{\mathbf{k}}$	Unit vectors in x, y, z directions
$\mathbf{b}$	Electromagnetic field induced by ocean current
$\mathbf{V}$	Ocean current velocity
$\mathbf{F}$	Earth's geomagnetic field
σ	Electrical conductivity
Φ	Electric field potential
$\mathbf{V}_{\mathrm{sgw}}$	Surface waves' velocity
σ_{u0}^2	Horizontal velocity variance of the surface wave at the ocean surface
ψ	Phase of the surface waves
k_x and k_y	Wavenumber components in x and y directions, respectively
ϕ_0	Initial phase of the surface wave (at $x = 0$, $y = 0$, and $t = 0$)
θ	Surface wave propagation direction counterclockwise from the east
f	Surface waves' frequency
ω	Surface waves' angular frequency
k	Wavenumber magnitude
$\mathbf{J}'$	Electric current induced by surface waves
$\overline{\left(\frac{J_x}{\sigma}\right)^*}$ and $\overline{\left(\frac{J_y}{\sigma}\right)^*}$	All depth-independent electric current terms in Sanford et al. (1978)
β	Geomagnetic field inclination effect
$\overline{J}$	Electric current induced by a low-frequency ocean current (appendix A, section d)
EM-APEX float estimated surface waves	
$-\nabla\Phi_{\mathrm{EM}}$	Electric field around EM-APEX floats
$\widetilde{\sigma_u}^2$	Profiles of velocity variance measured by EM-APEX floats
$\widetilde{f_p}$ and $\widetilde{H_s}$	Estimates of f_p and H_s using $\widetilde{\sigma_u}^2$ assuming the JONSWAP spectrum
$\breve{f}_p$ and $\breve{H}_s$	Estimates of f_p and H_s using $\widetilde{\sigma_u}^2$ assuming the single dominant surface wave following Sanford et al. (2011)
Ω	EM-APEX float angular rotation frequency
ϕ_i	Orientation of the two pairs of electrodes at $t = 0$ (Fig. 2)
t	Time in the 50-s harmonic fit
α	Rotational demodulation effect
Surface wave spectrum in the least squares fitting	
S_η	Surface wave spectral energy
S_p	Peak spectrum level of S_η at f_p
σ_a, σ_b, and γ	Dimensionless shape parameters in the JONSWAP spectrum
f_p	Peak frequency
H_s	Significant wave height
$\widehat{\sigma_u}^2$	Modeled velocity variance of surface waves using empirical surface wave spectrum S_η
WAVEWATCH III model (ww3)	
σ_{ww3}^2	ww3 simulations of surface waves' horizontal velocity variance
$\widetilde{\sigma_{\mathrm{ww3}}}^2$	Simulations of σ_{ww3}^2 measured by EM-APEX floats
$\widetilde{f_p}^{\mathrm{ww3}}$ and $\widetilde{H_s}^{\mathrm{ww3}}$	Estimates of f_p and H_s using $\widetilde{\sigma_{\mathrm{ww3}}}^2$
f_p^{ww3} and H_s^{ww3}	ww3 model output of f_p and H_s
S_η^{ww3}	ww3 model output of S_η
Notations in the appendixes	
$\mathbf{E}$	Background electric field
$\mathbf{B}$	Ambient magnetic field
$\mathbf{a}$	Magnetic vector potential
$\mathbf{b}$	Electromagnetic field
μ	Magnetic permeability
η	Sea surface displacement

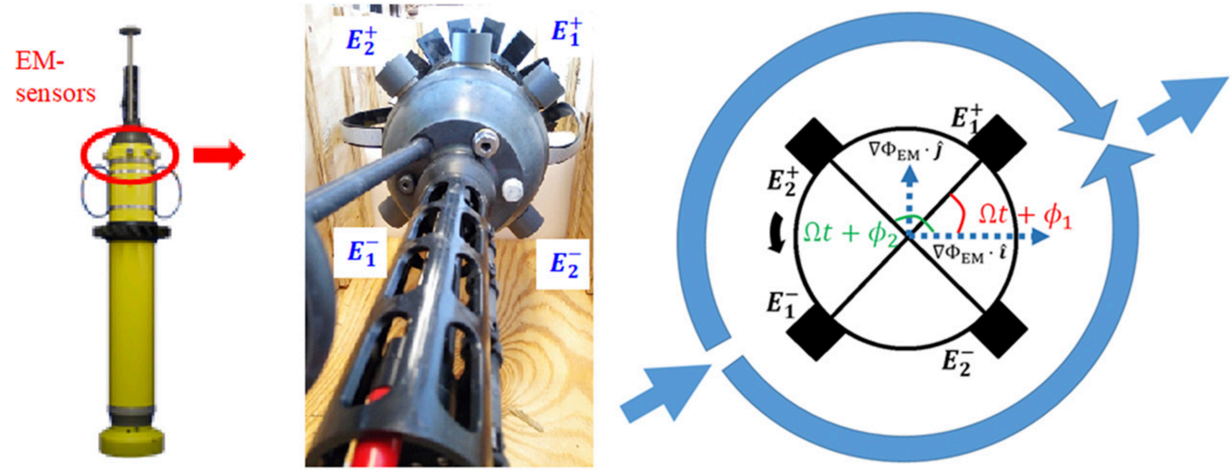

FIG. 2. (left) Photo of EM-APEX floats, (middle) the top view of EM-APEX floats, and (right) an illustration of electric field around floats, $-\nabla\Phi_{EM}$ (blue arrows). The voltage measured by two orthogonal pairs of electrodes, E_1 and E_2, is associated with $\nabla\Phi_{EM}$ The float rotates counterclockwise viewed from the top when ascending, at a rotation angular frequency Ω (black arrow). The angle between the pair of electrodes E_i and the magnetic east is $\Omega t + \phi_i$ ($i = 1$ for the E_1 pair and $i = 2$ for the E_2 pair). The projection of $\nabla\Phi_{EM}$ on E_i is equal to $(\nabla\Phi_{EM}\cdot\hat{\imath})\cos(\Omega t+\phi_i) + (\nabla\Phi_{EM}\cdot\hat{\jmath})\sin(\Omega t+\phi_i)$, where t is time and ϕ_i is the initial phase at $t = 0$.

EM-APEX floats is about $0.11\,\mathrm{m\,s^{-1}}$, which is slightly faster descending than ascending ($\sim 0.02\,\mathrm{m\,s^{-1}}$ difference).

EM-APEX floats measure the voltage using two pairs of Ag-AgCl electrodes (Fig. 2), E_1 and E_2 pairs, mounted on orthogonal axes (Sanford et al. 2005). The sampling rate of voltage is 1 Hz. As the floats profile vertically, they rotate by an array of slanted blades mounted on the float. The rotation frequency is about 0.08 Hz when the floats ascend and 0.12 Hz when the floats descend. Oceanic horizontal currents are estimated by least squares fitting every 50 s of the float voltage measurements (Sanford et al. 1978) with a moving window of 25 s; that is, the raw voltage data size is 25 times larger than the processed current velocity data. The residual squares from the harmonic fit represent the velocity variance of surface waves plus measurement errors $\widetilde{\sigma_u}^2$ (details in section 4). Float GPS positions and measurements of salinity, temperature, horizontal current velocity, and velocity variance are transmitted via Iridium satellite communications when the floats surface. The raw voltage data cannot be collected via satellite because of size, but they could be downloaded from the floats after recovery by ship.

Four EM-APEX floats measured velocity variances at wind speeds $> 25\,\mathrm{m\,s^{-1}}$ under Typhoon Fanapi (magenta dots in Fig. 1). The $\widetilde{\sigma_u}^2$ decayed "exponentially" with depth (Figs. 3e–h), in agreement with the report by Sanford et al. (2011). air pump tubing inside the floats used to inflate air bags was broken due to strong Fanapi downwelling winds, resulting in the floats descending from the sea surface slower than usual in the first several minutes and thereby lengthening the rotation period for measuring voltage. Voltage measured by the electrodes with a rotation period > 25 s was excluded from the data processing (Sanford et al. 2005), so 38% of profiles of $\widetilde{\sigma_u}^2$ have no measurements in the upper 20 m. The $\widetilde{\sigma_u}^2$ is used to estimate surface wave properties in this study (section 5).

3. Theory of seawater motion-induced electric current

a. Electric current in a moving medium

Sanford (1971) studies the motional induction of oceanic current modulated by the electromagnetic field **b** in Earth's geomagnetic field (appendix A, section a). Because the temporal variations of **b** and the motional induction of ocean current in the **b** affect the electric field insignificantly, the electric current induced by a low-frequency ocean current is mainly driven by the motional induction resulting from the ocean current **V** crossing Earth's geomagnetic field **F** (Longuet-Higgins et al. 1954) and the background electric field $-\nabla\Phi$, that is,

$$\frac{\mathbf{J}}{\sigma} \approx -\nabla\Phi + \mathbf{V}\times\mathbf{F}, \tag{1}$$

where $\mathbf{J} = J_x\hat{\mathbf{i}} + J_y\hat{\mathbf{j}} + J_z\hat{\mathbf{k}}$, $\mathbf{V} = u\hat{\mathbf{i}} + v\hat{\mathbf{j}} + w\hat{\mathbf{k}}$, and $\mathbf{F} = F_y\hat{\mathbf{j}} + F_z\hat{\mathbf{k}}$ (Table 1). Equation (1) can also be applied to the electric current induced by a surface wave, because the electromagnetic field induced by surface waves affects the electric field negligibly (appendix A, section b; Weaver 1965).

b. Electric current induced by a surface wave and low-frequency current in the upper ocean

Sanford et al. (1978) shows that the electric current induced by a low-frequency ocean current $\mathbf{u} = u\hat{\mathbf{i}} + v\hat{\mathbf{j}}$

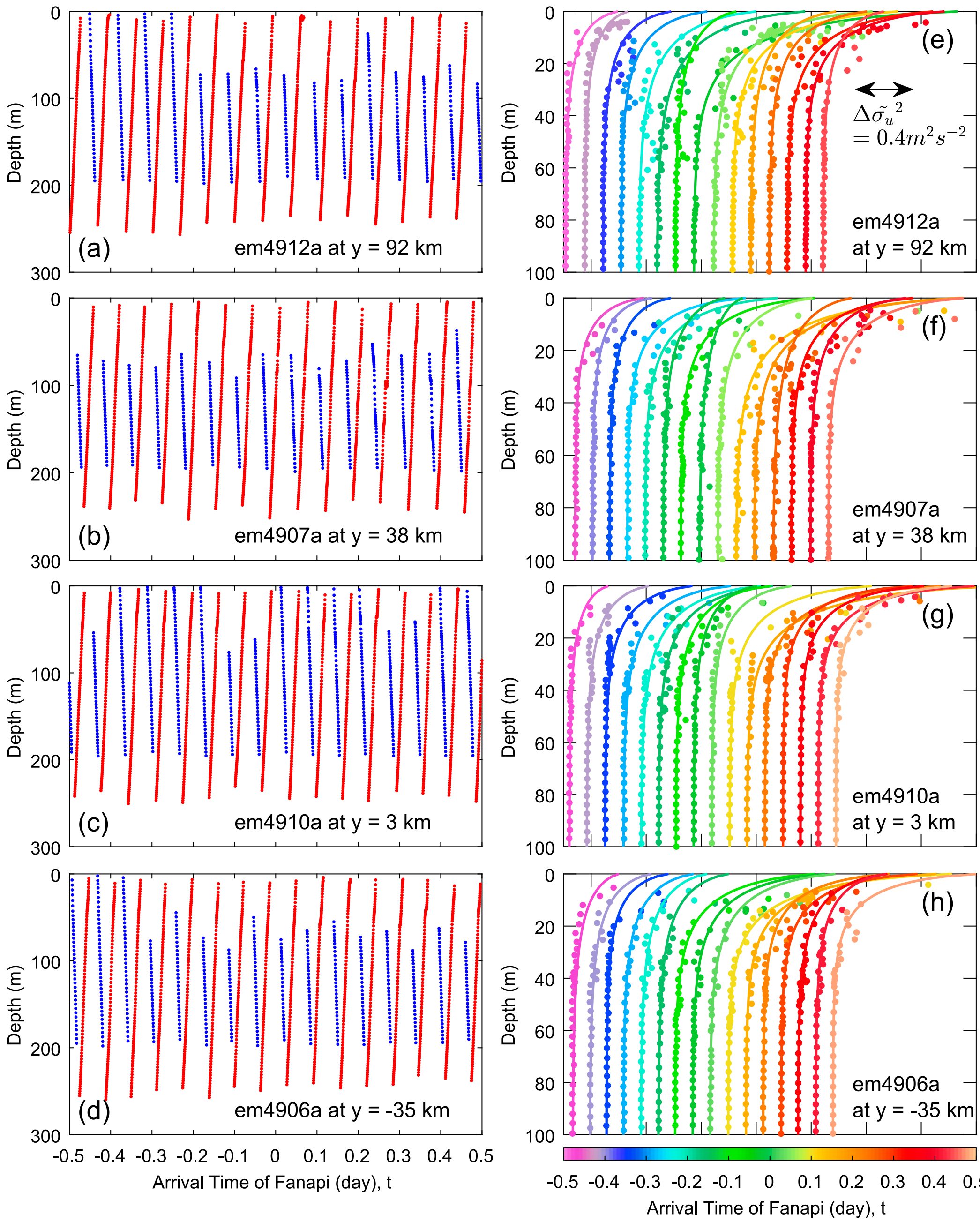

FIG. 3. (a)–(d)Vertical positions of four EM-APEX floats near Fanapi's track descending (blue dots) and ascending (red dots). (e)–(h) The profiles of measured velocity variance $\widetilde{\sigma_u}^2$ taken by one pair of the electrodes E_1 on the floats ascending (dots) at the time relative to the arrival time of Typhoon Fanapi's eye at the float array (different colors). The abscissa in (a)–(d) is the time t relative to the arrival time of Typhoon Fanapi's eye at the float array, 0130 UTC 18 Sep 2010. The scale of $\Delta\widetilde{\sigma_u}^2$ is presented in (e). Colored curves in (e)–(h) are The estimated surface wave profiles are shown in (e)–(h) using the method described in section 4 (colored curves). The average float distance to Fanapi's track is labeled in the lower-right corner in each panel, with the positive values to the right-hand side of the track.

[Eq. (A10) in appendix A, section c], assuming a negligible horizontal shear of $\mathbf{u}$. If the surface wave velocity $\mathbf{V}_{\mathrm{sgw}}$ [Eq. (A11)] is assumed to induce the electric current $\mathbf{J}'$ in the same as the low-frequency current (the superscript prime ($'$) represents the wave-induced component), then $\mathbf{J}'$ can be expressed as

$$\mathbf{J}'/\sigma \approx \sqrt{2}\sigma_{u0}F_z \sin\psi(\sin\theta\hat{\mathbf{i}} - \cos\theta\hat{\mathbf{j}})\, e^{kz} + \left[\overline{\left(\frac{J_x}{\sigma}\right)}^{*}\hat{\mathbf{i}} + \overline{\left(\frac{J_y}{\sigma}\right)}^{*}\hat{\mathbf{j}}\right], \qquad (2)$$

where $\psi = k_x x + k_y y - \omega t + \phi_0$, $\theta = \tan^{-1}(k_y/k_x)$, and $\mathrm{k} = (k_x^2 + k_y^2)^{\frac{1}{2}}$. The $\mathbf{J}'$ is affected by the surface wave velocity amplitude ($\sigma_{u0}\, e^{kz}$) at different depths.

We assume the locally uniform conductivity σ in the upper ocean, $\nabla(1/\sigma) = 0$; the conservation of electric current $\mathbf{J}$, $\nabla\cdot\mathbf{J} = 0$; the boundary condition $J_z \approx 0$ at the ocean surface $z = 0$ [Eq. (A13); Longuet-Higgins et al. 1954); and the boundary condition $\Phi \approx 0$ at $z = -\infty$ [Eq. (A14)]. Using the abovementioned assumptions and the boundary conditions in Eq. (1), the electric current $\mathbf{J}' = J_x'\hat{\mathbf{i}} + J_y'\hat{\mathbf{j}}$ induced by a single surface wave in the deep ocean is [Eq. (A17) in appendix A, section d)

$$\mathbf{J}'/\sigma = \sqrt{2}\sigma_{u0}F_z\sqrt{1+\beta^2}\sin\psi_\omega(\sin\theta\hat{\mathbf{i}} - \cos\theta\hat{\mathbf{j}})e^{kz}, \qquad (3)$$

where $\psi_\omega = \psi + \tan^{-1}(\beta)$ and the geomagnetic field inclination effect $\beta = (F_y/F_z)\sin\theta$. Compared with Eq. (2), the amplitude and phase of $\mathbf{J}'$ are modified for the geomagnetic field inclination F_y/F_z and surface wave propagation directionθ.

Assuming the interaction between the low-frequency current and surface waves in the motional induction resulting from the electromagnetic field is negligible, the electric current $\mathbf{J} = J_x\hat{\mathbf{i}} + J_y\hat{\mathbf{j}}$ induced by a low-frequency current and a surface wave in the upper ocean is

$$\begin{cases} \dfrac{J_x}{\sigma} = \dfrac{J_x'}{\sigma} + \dfrac{\overline{J}_x}{\sigma} = \sqrt{2}\sigma_{u0}F_z\sqrt{1+\beta^2}\sin\psi_\omega \sin\theta\, e^{kz} + \dfrac{\overline{J}_x}{\sigma} \\ \dfrac{J_y}{\sigma} = \dfrac{J_y'}{\sigma} + \dfrac{\overline{J}_y}{\sigma} = -(\sqrt{2}\,\sigma_{u0}F_z\sqrt{1+\beta^2}\,\sin\psi_\omega \cos\theta\, e^{kz}) + \dfrac{\overline{J}_y}{\sigma} \end{cases}. \qquad (4)$$

4. Methods to estimate surface waves using EM-APEX float measurements

a. *Profiles of high-frequency velocity variance $\widetilde{\sigma_u}^2$ measured by floats*

EM-APEX floats measure the voltage $\Delta\Phi$ associated with the electric field $-\nabla\Phi_{\mathrm{EM}}$ around the floats (Fig. 2), which is primarily from the electric current $\mathbf{J}$ [Eq. (4)] induced by the motional induction of seawater [Eq. (B3) in appendix B, section a]. Voltage measurements taken by two pairs of rotating electrodes E_1 and E_2 (appendix B, section b), $\Delta\Phi_i$ ($i = 1$ for the E_1 pair and $i = 2$ for the E_2 pair), are least squares fitted in 50-s data windows to demodulate the voltage associated with the low-frequency electric current $\overline{J}$ (<0.02 Hz) from the voltage measurement offset and trend (appendix B, section c; Sanford et al. 1978), because the offset and trend are much greater than $\overline{\mathbf{J}}$. The residuals ϵ_i in the harmonic fit contain part of the voltage associated with the wave-induced electric current $\mathbf{J}'$ (>0.02 Hz).

The residuals ϵ_i are used to provide the profiles of the estimated velocity variance $\widetilde{\sigma_u}^2$ [Eqs. (B6) and (B10) in appendix B, section d] as

$$\widetilde{\sigma_u}^2 \approx \frac{(1+\alpha)}{4}(1+\beta^2)\sigma_{u0}^2\, e^{2kz} + \delta^2, \qquad (5)$$

where $\alpha = 2\langle\cos^2\tilde{\psi}\rangle - 2\langle\cos\tilde{\psi}\rangle^2 - 2\langle\cos 2\psi_\Omega\rangle$ represents the rotational demodulation effect resulting from the difference between the surface wave angular frequency ω and the EM-APEX float angular rotation frequency Ω, $\tilde{\psi} = -(\omega - \Omega)t + \widetilde{\phi_0}$, $\widetilde{\phi_0} = k_x x + k_y y + \phi_0 + \phi_i + \tan^{-1}(\beta) - \theta$, $\psi_\Omega = \theta - \Omega t + \phi_i$, where the angle brackets, $\langle\,\rangle$, represent the average over the 50-s fitting window ($\Delta T = 50$), and δ^2 is the instrumental noise ($\delta = 0.8$–$1.5\,\mathrm{cm\,s^{-1}}$ in Hsu et al. 2017).

Estimated velocity variance may differ from the actual surface wave velocity variance ($\sigma_{u0}^2\, e^{2kz}$) as a result of the rotational demodulation effect α and the geomagnetic field inclination effect β [Eq. (5)], biasing surface wave estimates. The α is always less than 1 for surface waves and low-frequency current when the float rotation rate $\Omega \geq \Omega_c$, where $\Omega_c = 2\pi/\Delta T\ \mathrm{rad\,s^{-1}}$. Typically, float $\Omega \approx 4\Omega_c$ when ascending. The $2\langle\cos\tilde{\psi}\rangle^2$ in the expression of α, associated with the mean of surface wave measurements on the rotating electrodes, is removed as the offset in the processing of voltage measurements [Eq. (B5)] and may not be zero if $|\omega - \Omega|/2\pi <$ 0.02 Hz. So, $\alpha = 0$–1. The F_y and F_z were about 36 and $-24\ \mu T$, respectively, under Typhoon Fanapi, according to the geomagnetic field data from the NOAA National Centers for Environmental Information (NCEI) (Thébault et al. 2015), that is, $\beta^2 \leq 2.25$.

In short, the α effect may underestimate the actual surface wave velocity variance by 50%–75% ($\alpha = 0$–1), and the β effect may overestimate by >2 times ($\beta^2 =$ 2.25). Sanford et al. (2011) neglect the α and β effects when estimating surface waves, assuming a single dominant surface wave velocity variance as $\widetilde{\sigma_u}^2 = \sigma_{u0}^2\, e^{2kz}$.

In this study we use the profiles of $\widetilde{\sigma_u}^2$ to estimate surface waves, assuming a broadband surface wave spectrum, including corrections of the α and β effects (section 5a), instead of following Sanford et al. (2011). The results from two different approaches will be compared in section 5b.

b. Estimating surface waves from velocity variance profiles

Surface wave spectra S_η under tropical cyclones have been reported previously (Ochi and Chiu 1982; Young 1998; Ochi 2003; Young 2003). Over 85% of surface waves under hurricanes have a single peak frequency spectrum (Hu and Chen 2011), similar to the empirical JONSWAP surface wave spectrum (Young 1998). The remaining 15% of surface waves have two frequency spectral peaks.

We assume that surface wave spectra under Typhoon Fanapi can be parameterized by the empirical JONSWAP spectrum form $S_\eta(f_p, S_p, \sigma_a, \sigma_b, \gamma)$ [Eq. (D1)], where S_p is the peak spectrum level of S_η at the peak frequency f_p; and σ_a, σ_b, and γ are the dimensionless shape parameters. This assumption should be reliable to most wind waves in the open ocean. We further assume constant shape parameters σ_a, σ_b, and γ, so that $S_\eta = f(f_p, S_p)$. Modeled velocity variance $\widehat{\sigma_u}^2(S_\eta, z)$ of surface waves depends on only f_p and S_p (appendix C), that is, $\widehat{\sigma_u}^2(S_\eta, z) = \widehat{\sigma_u}^2(f_p, S_p, z)$.

The parameters $\widetilde{f_p}$ and $\widetilde{S_p}$ are estimated by minimizing the root-mean-square logarithmic error (RMSLE) between observed velocity variance $\widetilde{\sigma_u}^2(z)$ [Eq. (5)] corrected by an estimated instrument error δ^2 and modeled velocity variance $\widehat{\sigma_u}^2(f_p, S_p, z)$,

$$\mathrm{RMSLE}(f_p, S_p) = \sqrt{\frac{\sum_{i=1}^{N} \left\{\log[\widetilde{\sigma_u}^2(z_i) - \delta^2] - \log[\widehat{\sigma_u}^2(f_p, S_p, z_i)]\right\}^2}{N}}, \tag{6}$$

where N is the number of $\widetilde{\sigma_u}^2$ measurements in the upper 100 m (~31 data points when floats ascend) and δ^2 is estimated as the average of observed $\widetilde{\sigma_u}^2(z)$ between 150 and 200 m, assuming that surface wave signals are negligible within this layer. The $\widetilde{S_\eta}$ is estimated using $\widetilde{f_p}$ and $\widetilde{S_p}$ [Eq. (D1)]. Confidence intervals of surface wave estimates are evaluated using the bootstrapping method (Roy 1994). We randomly select 80% of the $\widetilde{\sigma_u}^2$ measurements in each profile to estimate surface waves and repeat 100 times. The results of the 100 realizations are used to compute the mean and standard deviation of surface wave estimates.

Significant wave height $\widetilde{H_s}$ is estimated using $\widetilde{S_\eta}$, assuming a Rayleigh distribution of surface waves (Young 1999),

$$\widetilde{H_s} \approx 4\widetilde{\sigma_\eta} = 4\sqrt{\int \widetilde{S_\eta}\, df}, \tag{7}$$

where $\widetilde{\sigma_\eta}^2$ is the estimated variance of ocean surface displacements.

5. Surface waves under Typhoon Fanapi 2010

a. Surface wave estimates assuming the JONSWAP spectrum

The peak frequency $\widetilde{f_p}$ and significant wave height $\widetilde{H_s}$ are estimated using the observed velocity variance $\widetilde{\sigma_u}^2$ in the upper 100 m (Figs. 3e–h), assuming the JONSWAP spectrum [$\sigma_a = 0.07$, $\sigma_b = 0.09$ and $\gamma = 3.3$ in Eq. (D1)]. Three successive profiles of $\widetilde{\sigma_u}^2$ taken within 1.5 h are used in the fitting to reduce errors in estimates. We exclude profiles with no measurements in the upper 20 m (the profiles of blue dots in Fig. 3, ~38%), because the surface wave exponential depth-decaying scale (g/ω^2) is less than 20 m at frequencies > 0.12 Hz, where g is gravity.

The sum of $\widetilde{\sigma_u}^2$ [Eq. (5)] from the orthogonal E_1 and E_2 may not equal the actual surface wave velocity variance, because some variance in surface waves might have been removed as the offset in the data processing on each pair of electrodes [Eq. (B5)]. In this study the surface waves are estimated using measurements on E_1 and E_2 separately. The α effect on the estimated $\widetilde{H_s}$ is corrected using an empirical corrected function (section 7c), derived using the simulated surface waves under Typhoon Fanapi in the ww3 model (section 6), assuming a random distribution of initial surface wave phase. The β effect on $\widetilde{H_s}$ is corrected using the ww3 model output of surface wave propagation direction at f_p (section 7d).

Estimates of $\widetilde{f_p}$ and $\widetilde{H_s}$ under Typhoon Fanapi using estimated $\widetilde{\sigma_u}^2$ taken by two independent pairs of electrodes on each float agree with each other (Fig. 4). The mean and standard deviation of all fitted profiles' RMSLE [Eq. (6)] is ~0.048 ± 0.017. At 0.4 day before the arrival of Typhoon Fanapi's eye, the $\widetilde{f_p}$ is about 0.07–0.08 Hz and remains nearly constant until the passage of Fanapi. The $\widetilde{H_s}$ on the right-hand side of Fanapi's track is mostly

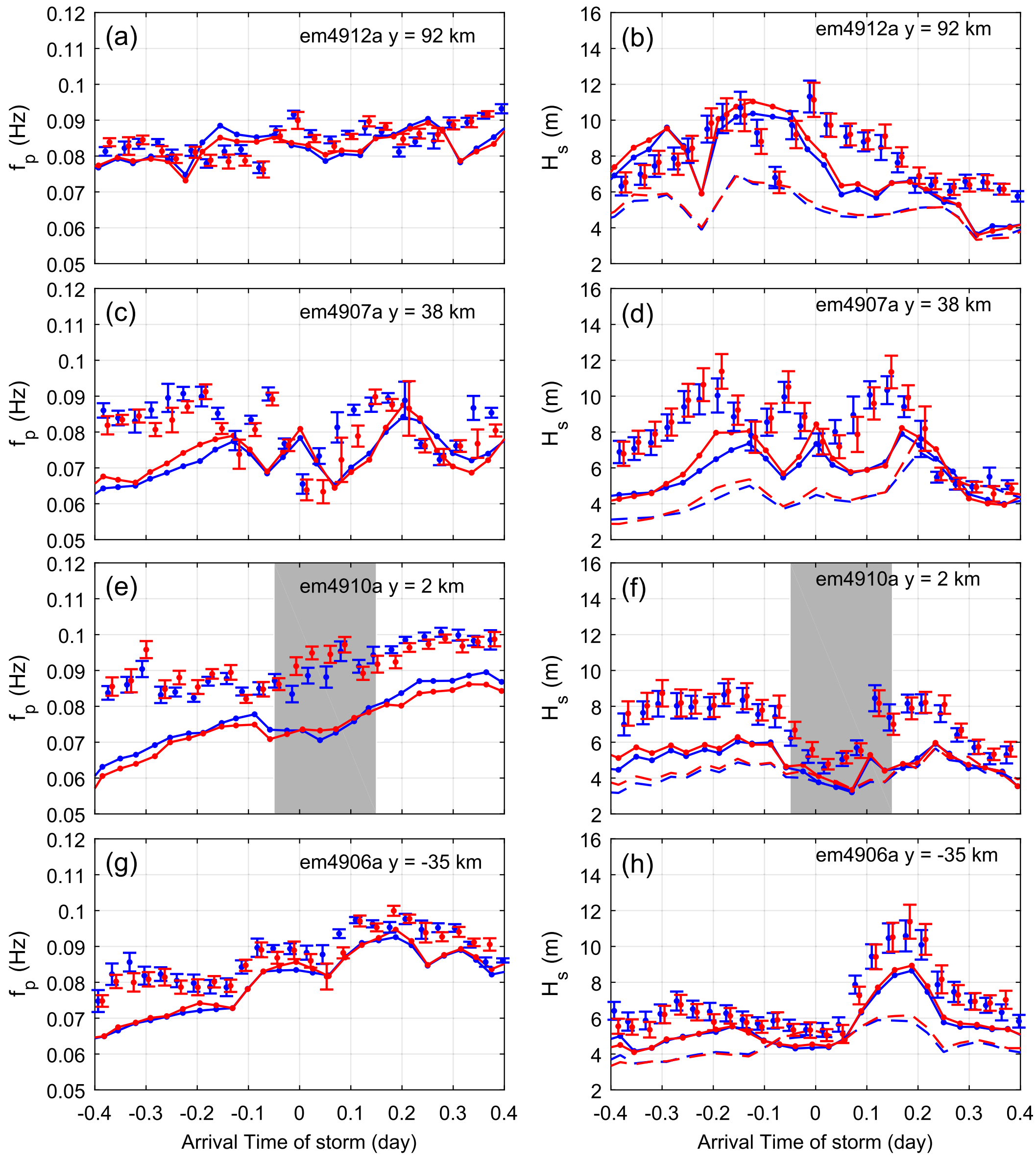

FIG. 4. EM-APEX float estimates of (a),(c),(e),(g) peak frequency and (b),(d),(f),(h) significant wave height assuming the JONSWAP spectrum ($\widetilde{f}_p$ and $\widetilde{H}_s$, respectively; dots with error bars as one standard deviation) or assuming a single dominant surface wave ($\breve{f}_p$ and $\breve{H}_s$, respectively; dots connected with lines) on electrodes E_1 (blue) and E_2 (red) of four EM-APEX floats. Also shown is $\breve{H}_s$ without the correction of α and β effects (dashed lines). The average float distance to Fanapi's track is labeled in the upper-right corner of each panel, with positive values to the right-hand side of the track. Poor surface wave estimates within Fanapi's eyewall resulting from the assumption of the JONSWAP spectrum (shaded gray area; see Fig. 6).

6–10 m before the passage of Fanapi's eye. The $\widetilde{H}_s$ at the front-left quadrant of Fanapi is about 6 m and sometimes it is 5 m lower than at the front-right quadrant. After the eye of Typhoon Fanapi passes the float array, $\widetilde{f}_p$ changes from 0.08 to 0.1 Hz at floats em4906a (left) and em4910a (track), and about 0.08 ± 0.01 Hz on the right-hand side of the track (em4907a and em4912a). The maximum $\widetilde{H}_s$ at the rear-left quadrant of Typhoon Fanapi is about 11 m at 0.15 day after the eye of Typhoon Fanapi passed the float (em4906a), nearly the same as that at the rear-right quadrant (em4907a).

The $\widetilde{f}_p$ at the rear-left quadrant of Fanapi is higher than at the front-right quadrant, supporting the spatial variability reported in previous model studies (e.g., Moon et al. 2004; Fan et al. 2009). The $\widetilde{H}_s > 10$ m at the rear-left quadrant of Fanapi is higher than reported in studies using SRAs under hurricanes (e.g., Wright et al. 2001; Fan et al. 2009). Because the RMSLE at the rear-left quadrant of Fanapi, ~0.043, is within the 95% confidence interval, the nonlinear fitted results using the assumption of the JONSWAP spectrum may still be reliable. Note that Fanapi's translation speed U_h is $\sim 4\,\mathrm{m\,s^{-1}}$. The slow motion of Fanapi may reduce the "extended fetch" effect (Young 2003) and results in more symmetric $\widetilde{H_s}$ at the rear sector of Fanapi than other storms, for example, $U_h \sim 5\,\mathrm{m\,s^{-1}}$ in Hurricane Ivan (from NHC best-track data). Collins (2014) also estimates the surface waves under Fanapi, but the wave measurements on the nearest buoy were >300 km to the left-hand side of Fanapi's track; they are not used as comparisons in the present study.

b. *Surface wave estimates assuming a single dominant surface wave*

Sanford et al. (2011) assume that the estimated velocity variance $\widetilde{\sigma_u}^2$ equals a single dominant surface wave's velocity variance, $\widetilde{\sigma_u}^2 = \sigma_{u0}^2 e^{2kz}$, and linearly least squares fit the observed profiles of $\widetilde{\sigma_u}^2$ to derive wavenumber k and σ_{u0}^2 in the logarithmical scale, that is, $\log[\widetilde{\sigma_u}^2(z)] = 2kz + \log(\sigma_{u0}^2)$. The peak frequency $\breve{f}_p = (2\pi)^{-1}(gk)^{1/2}$ and the significant wave height $\breve{H}_s = 4\sigma_{u0}(gk)^{-1/2}$ are computed using estimated k and σ_{u0}^2 (Fig. 4). The $\breve{H}_s$ is corrected for the α effect according to Eq. (5) and for β effects using the ww3 model output (section 7d). The difference in $\breve{H}_s$ as a result of the α and β effects can be more than 3 m (dashed lines vs sold lines with dots in Fig. 4), unless these two effects (α: underestimated; β: overestimated) were coincidentally balanced by each other; that is, corrections for α and β effects are required.

Estimates of $\breve{f}_p$ and $\breve{H}_s$ are compared with $\widetilde{f_p}$ and $\widetilde{\mathrm{H_s}}$, respectively, using the JONSWAP spectrum (dots with error bars vs sold lines with dots in Fig. 4). At the positions of floats em4907a and em4906a (~40 km off Fanapi's track; Figs. 4c and 4g), the $\breve{f}_p$ is >0.01 Hz lower than $\widetilde{f_p}$ at 0.2 day before the passage of Fanapi's eye and is <0.01 Hz lower than $\widetilde{f_p}$ after the passage of the eye. The $\breve{H}_s$ on the left-hand side of Fanapi's track is about 1–2 m lower than $\widetilde{\mathrm{H_s}}$, but it is mostly more than 3 m lower than at floats em4907a (right) and em4910a (track). The difference between $\breve{f}_p$ and $\widetilde{f_p}$ is less than 0.01 Hz at 92 km on the right-hand side of Fanapi's track (em4912a; Fig. 4a) and more than 50% of $\breve{H}_s$ differ from the $\widetilde{\mathrm{H_s}}$ within 2 m. The difference in surface wave estimates is due to the assumption of a surface wave spectrum, that is, broad band versus narrow band.

6. Surface waves simulations under Typhoon Fanapi in ww3

The WAVEWATCH III oceanic surface wave model, version 5.16 (WAVEWATCH III Development Group 2016), developed by the NOAA National Centers for Environmental Predication (NCEP), has been used in studies of global and regional surface wave forecasts (e.g., Moon et al. 2004; Reichl et al. 2014). In this study we simulate surface waves under Typhoon Fanapi using ww3 (section 6a) for several purposes: 1) to compare directly surface waves derived from floats with those from ww3 model simulations (section 6b), 2) to justify the uncertainties of float estimates of surface waves resulting from the assumption of the JONSWAP spectrum (sections 7a and 7b), and 3) to quantify the biases of float estimates of surface waves caused by the aliasing effect α (section 7c) and the geomagnetic field inclination effect β (section 7d).

a. *Simulated surface waves during Typhoon Fanapi in the ww3*

The surface wave field under Typhoon Fanapi is simulated in the ww3 model from 0100 UTC 17 September to 1200 UTC 18 September (Fig. 5), using the model results of Typhoon Fanapi winds (appendix E). The simulated directional surface wavenumber spectra are discretized in 24 directions of 15° intervals and 45 frequencies from 0.012 to 1.3 Hz at a logarithmic increment $f_{n+1} = 1.1 f_n$, following previously described methods (e.g., Moon et al. 2004; Fan et al. 2009; Reichl et al. 2014). The model includes wind forcing, wave–wave interaction, and the dissipation resulting from whitecapping and wave–bottom interaction. The wind forcing is parameterized in the ST2 package following Tolman and Chalikov (1996) (WAVEWATCH III Development Group 2016). The drag coefficient cap is set at 2.5×10^{-3}, occurring at wind speed $> 30\,\mathrm{m\,s^{-1}}$. The nonlinear wave–wave interaction is simulated using the discrete interaction approximation (Hasselmann et al. 1985). The temporal resolution is 180 s, and the spatial resolution is 0.1° latitude × 0.1° longitude. The water depth is obtained from NOAA NCEI in the western Pacific.

At the front-right quadrant of Fanapi, simulated surface waves are longer and higher than waves at the rear-left quadrant, a pattern consistent with the simulated and observed surface wave fields under other tropical cyclones (Wright et al. 2001; Moon et al. 2004; Chen et al. 2013). The simulated propagating directions of surface waves in different quadrants also agree qualitatively with those observed under other tropical cyclones (Wright et al. 2001; Young 2006; Potter et al. 2015), that is, propagating nearly perpendicular to the wind at the front-left quadrant of the typhoon and nearly parallel with the wind at the right-hand side of the storm's track.

Black et al. (2007) and Holthuijsen et al. (2012) define three sectors to describe the surface wave fields under tropical cyclones—front-left, right, and rear sectors—based on reported observations of surface wave

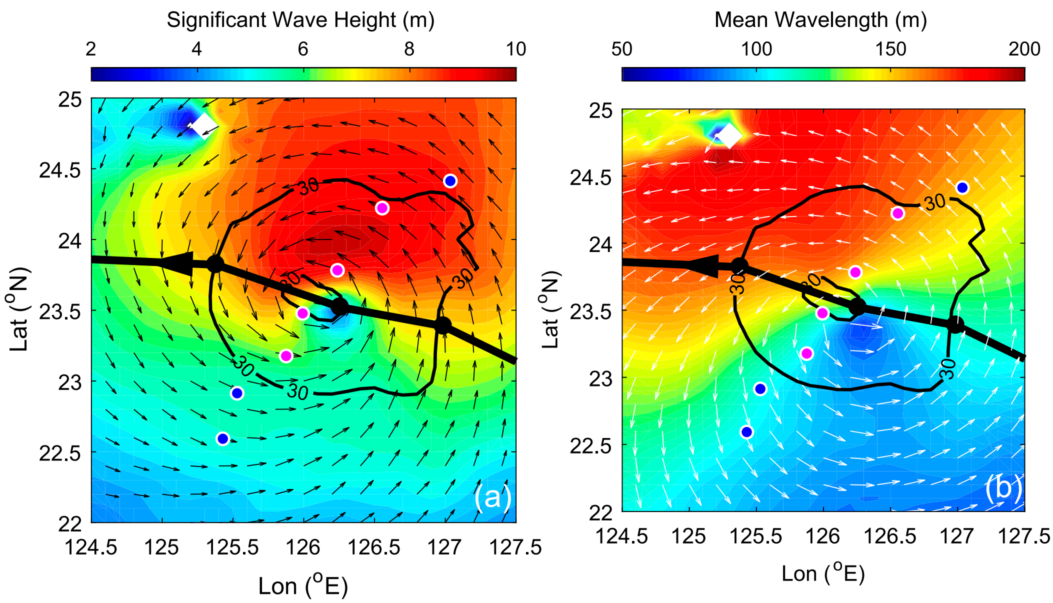

FIG. 5. WAVEWATCH III (ww3) model outputs of (left) significant wave height (color shading), (right) surface wave mean wavelength (color shading), and surface wave propagating direction (white arrows in the right panel) at 0130 UTC 18 Sep 2010 forced by the modeled Typhoon Fanapi winds (black contour lines and black arrows in the left panel). The ww3 model results for surface waves at the EM-APEX float positions (e.g., blue and magenta dots) are used for the discussion of float estimated surface waves in this study. Typhoon Fanapi moved nearly westward (black thick line).

propagation directions relative to the wind. Frequency spectra of ocean surface displacement S_η^{ww3} in the ww3 model simulation show a similar single peak broadband structure in the three sectors (Figs. 6b–d), except that the spectrum shows double peaks within the eyewall of the typhoon (Fig. 6e), presumably resulting from the

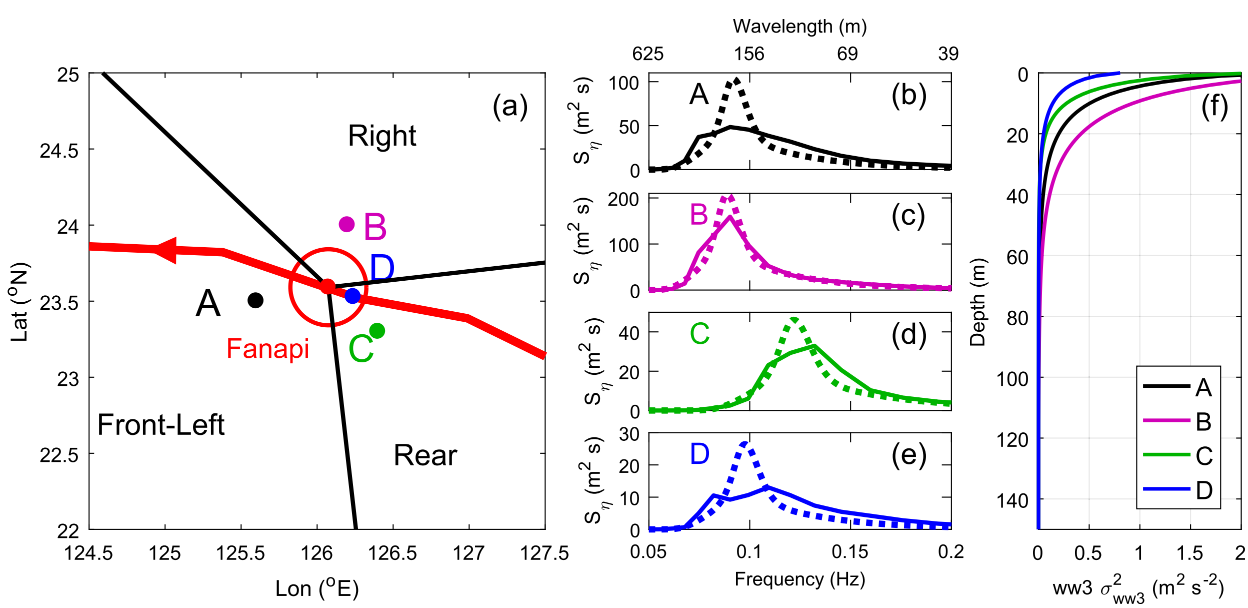

FIG. 6. (b)–(e) WAVEWATCH III model outputs of frequency spectrum of ocean surface displacement S_η^{ww3} (solid lines) at (a) four locations under Typhoon Fanapi: front-left (represented by black A), right (represented by purple B), and rear (represented by green C), and within the eyewall (represented by blue D within the red circle). Fitted results assuming the JONSWAP spectrum (dashed lines). Typhoon Fanapi (red dot) moves along the storm's track (red line) in the model. Profiles of σ^2_{ww3} are computed [Eq. (C2)] using the ww3 model results of surface wave spectra S_η^{ww3} at different locations [colored lines in (f)].

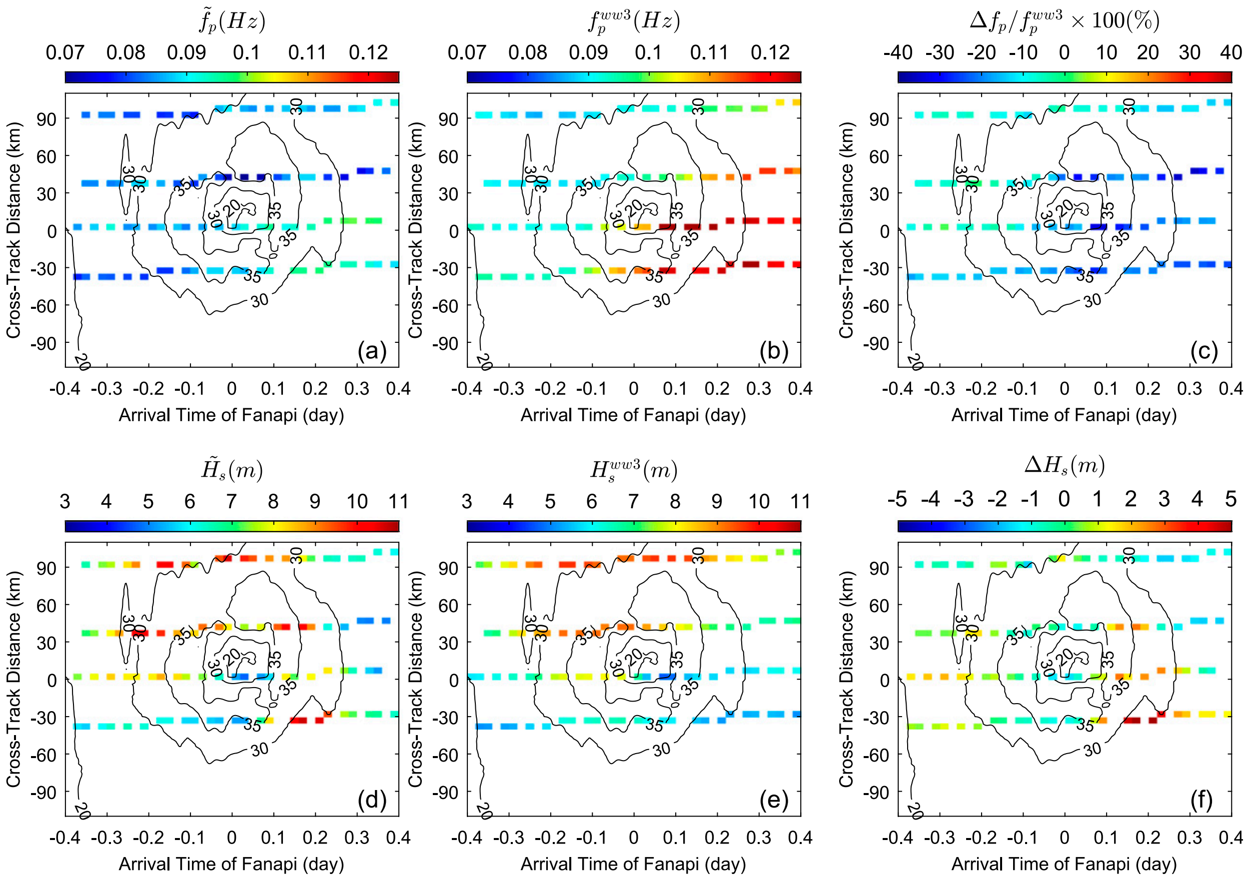

FIG. 7. Maps of (a) $\widetilde{f_p}$ and (d) $\widetilde{H_s}$ using results in Fig. 4, and actual ww3 model outputs of (b) f_p^{ww3} and (e) H_s^{ww3}. (c) The ratio $\Delta f_p/f_p^{\mathrm{ww3}}$ ($\Delta f_p = \widetilde{f_p} - f_p^{\mathrm{ww3}}$) and (f) ΔH_s ($\Delta H_s = \widetilde{H_s} - H_s^{\mathrm{ww3}}$). The wind speed at 10-m height above the sea surface (black contour lines). Abscissa shows the relative arrival time of Typhoon Fanapi's eye to the float array. The ordinate is the distance of float positions to Fanapi's track.

complicated nonlinear wave–wave interactions suggested by Hu and Chen (2011). Surface waves have higher values of maximum spectral energy level S_p and H_s in the right sector of Typhoon Fanapi (Figs. 5 and 6c). The S_η^{ww3} is used to compute the vertical profiles of surface wave velocity variance σ_{ww3}^2 [Eq. (C2)]. The σ_{ww3}^2 of surface waves with a shorter mean wavelength in the rear sector of Typhoon Fanapi decays more rapidly with depth than in the right sector (Figs. 5 and 6f).

b. Comparison between model results and float estimates

The ww3 model outputs of f_p^{ww3} and H_s^{ww3} are compared with $\widetilde{f_p}$ and $\widetilde{H_s}$, respectively, on the EM-APEX floats (Fig. 7). Before the arrival of Fanapi, f_p^{ww3} at all float positions is about 10% higher than $\widetilde{f_p}$ (Fig. 7c), consistent with the validation of ww3 by Fan et al. (2009). The H_s^{ww3} is in good agreement with $\widetilde{H_s}$, with a difference of <2 m (Fig. 7f). After the passage of Typhoon Fanapi, f_p^{ww3} at ~40 km off the track differs >20% from $\widetilde{f_p}$. The difference between The H_s^{ww3} and $\widetilde{H_s}$ on the right-hand side of Fanapi's track is mostly within 2 m, in agreement with the validation of ww3 by Fan et al. (2009). Interestingly, the H_s^{ww3} at the rear-left quadrant of Fanapi can be >5 m lower than $\widetilde{H_s}$. Fan and Rogers (2016) present directional surface wave spectra under Hurricane Ivan using SRA measurements and make comparisons to the ww3 model simulations. The ww3 model underestimates/overestimates the spectral energy at the wind-wave/swell frequency at the rear sector of the hurricane. Better parameterizations of the surface wave physics at the rear-left quadrant of Fanapi in the ww3 model may be needed.

7. Simulations of float-estimated surface waves using ww3

a. JONSWAP model spectrum

Our method for estimating surface waves assumes the JONSWAP spectrum. The uncertainty resulting from this assumption is assessed using the simulated surface wave horizontal velocity variance $\sigma_{\mathrm{ww3}}^2(z)$ (Fig. 6f), computed using S_η^{ww3} [Eq. (C2)]. Assuming $\widetilde{\sigma_{\mathrm{ww3}}}^2 = \sigma_{\mathrm{ww3}}^2 + \delta^2$,

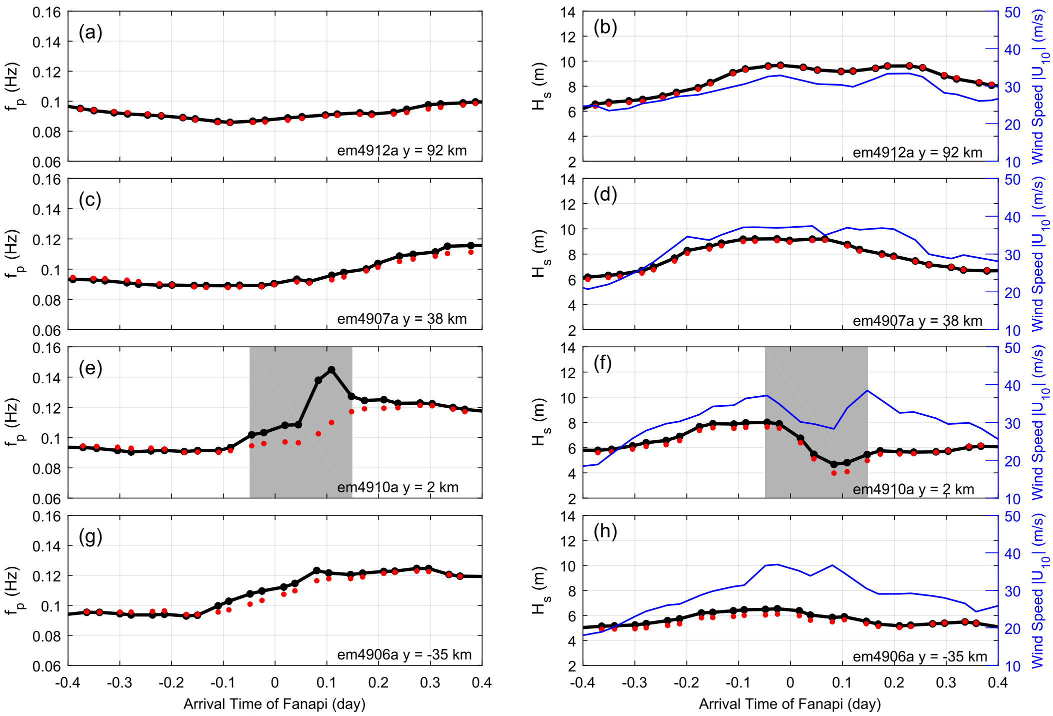

FIG. 8. Peak (a),(c),(e),(g) frequency $\widetilde{f_p}^{\mathrm{ww3}}$ and (b),(d),(f),(h) $\widetilde{H_s}^{\mathrm{ww3}}$ estimated using the ww3-simulated $\widetilde{\sigma_{\mathrm{ww3}}}^2$ (red dots), and the actual ww3 model outputs of f_p^{ww3} and H_s^{ww3} (black lines) at different float positions under Typhoon Fanapi. Average float distance to Fanapi's track is labeled in the lower-right corners of each panel, with the positive values to the right-hand side of the track. Wind speed $|\mathbf{U}_{10}|$ (blue lines) is labeled on the right-hand side of (b),(d), (f), and (h). Poor estimates of $\Delta f_p/f_p^{\mathrm{ww3}} > 5\%$ within Fanapi's eyewall (gray shading), resulting from the assumption of the JONSWAP spectrum, where $\Delta f_p = \widetilde{f_p}^{\mathrm{ww3}} - f_p^{\mathrm{ww3}}$.

$\widetilde{f_p}^{\mathrm{ww3}}$ and $\widetilde{H_s}^{\mathrm{ww3}}$ (superscript ww3 represents the simulated float estimates) are estimated using $\widetilde{\sigma_{\mathrm{ww3}}}^2$ in the upper 100 m, assuming the JONSWAP spectrum [$\sigma_a = 0.07$, $\sigma_b = 0.09$, and $\gamma = 3.3$ in Eq. (D1)]. The δ is assumed to be 1 cm s^{-1} (Hsu et al. 2017). The vertical resolution of $\widetilde{\sigma_{\mathrm{ww3}}}^2$ is 3 m, similar to the actual EM-APEX float measurements (~3 m).

The $\widetilde{f_p}^{\mathrm{ww3}}$ and $\widetilde{H_s}^{\mathrm{ww3}}$ are compared with the actual ww3 model outputs of f_p^{ww3} and H_s^{ww3} (Figs. 8 and 9). Most estimates of $\widetilde{f_p}^{\mathrm{ww3}}$ and $\widetilde{H_s}^{\mathrm{ww3}}$ (Figs. 9a and 9d) on the right-hand side of Typhoon Fanapi's track agree with the f_p^{ww3} and H_s^{ww3} (Figs. 9b and 9e), and the $\Delta f_p/f_p^{\mathrm{ww3}}$ ($\Delta f_p = \widetilde{f_p}^{\mathrm{ww3}} - f_p^{\mathrm{ww3}}$) and $\Delta H_s/H_s^{\mathrm{ww3}}$ ($\Delta H_s = \widetilde{H_s}^{\mathrm{ww3}} - H_s^{\mathrm{ww3}}$) are less than 2% (Figs. 9c and 9f). The S_η^{ww3} differs slightly from the fitted JONSWAP spectrum (Fig. 6c). The $\Delta f_p/f_p^{\mathrm{ww3}}$ and $\Delta H_s/H_s^{\mathrm{ww3}}$ on the left-hand side of the storm's track are larger but still within 5%, because the spectral peak of S_η^{ww3} (Fig. 6b) is broader than on the right-hand side of the track. Our analysis shows that $\widetilde{f_p}^{\mathrm{ww3}}$ and $\widetilde{H_s}^{\mathrm{ww3}}$ estimated assuming the JONSWAP spectrum are reliable outside the eyewall of Typhoon Fanapi—even the single spectral peak of the S_η^{ww3} is broader than the fitted JONSWAP spectrum. If the frequency of wind waves and swell on the left-hand side of the track is similar—for example, $f = 0.08$–0.10 Hz in Wright et al. (2001)—then the S_η computed by integrating bimodal "directional" spectra will remain a broader and monomodal spectrum feature.

However, within the eyewall of Typhoon Fanapi (gray shaded area in Figs. 8e and 8f), the $\Delta f_p/f_p^{\mathrm{ww3}}$ and $\Delta H_s/H_s^{\mathrm{ww3}}$ can be up to 25% and 14%, respectively, because the S_η^{ww3} has two spectral peaks within the eyewall (Fig. 6e). Our estimates using the float measurements within Fanapi's eyewall (e.g., gray shaded area in Figs. 4e and 4f) might not be reliable, because of the significant frequency difference between wind waves and swell.

b. *Variations of empirical spectrum*

We further evaluate the influence of variations in the spectral shape on surface wave estimates using $\widetilde{\sigma_{\mathrm{ww3}}}^2$. Donelan et al. (1985) propose a one-dimensional surface wave spectrum $S_\eta^*(f_p, S_p, |\mathbf{U}_{10}|)$ [Eq. (D2)]. The single spectral peak in S_η^* near the f_p is mainly parameterized by the peak enhancement factor γ_d (Young 1999), similar to the S_η of the JONSWAP spectrum [Eq. (D1)]. But, the spectral energy of S_η^* is proportional to f^{-4} at $f \gg f_p$, instead of f^{-5} in the S_η of the JONSWAP

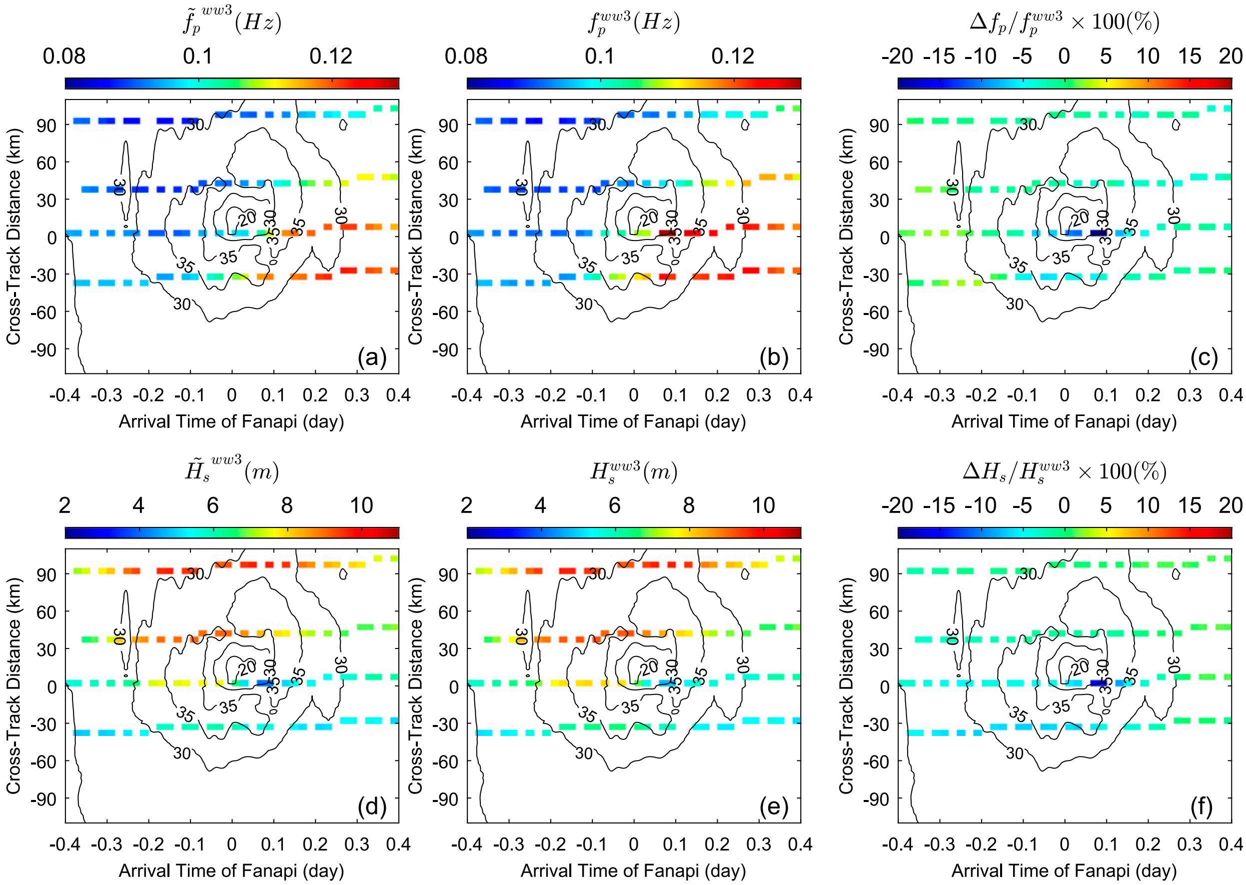

FIG. 9. Maps of ww3-estimated (a) $\widetilde{f_p}^{\mathrm{ww3}}$ and (d) $\widetilde{H_s}^{\mathrm{ww3}}$ using results in Fig. 8, and actual ww3 model outputs of (b) f_p^{ww3} and (e) H_s^{ww3}. The ratios (d) $\Delta f_p/f_p^{\mathrm{ww3}}$ and (f) $\Delta H_S/H_s^{\mathrm{ww3}}$, where $\Delta f_p = \widetilde{f_p}^{\mathrm{ww3}} - f_p^{\mathrm{ww3}}$ and $\Delta H_s = \widetilde{H_s}^{\mathrm{ww3}} - H_s^{\mathrm{ww3}}$, respectively. Wind speed $|\mathbf{U}_{10}|$ (black contour lines). The abscissa is the relative arrival time of Typhoon Fanapi's eye to the float array. The ordinate is the distance of float positions to Fanapi's track.

spectrum. The $\widetilde{f_p}^{\mathrm{ww3}}$ and $\widetilde{H_s}^{\mathrm{ww3}}$ estimated using S_η^* are nearly the same as those estimated using the JONSWAP spectrum (Fig. 10). The surface waves' spectral slope at high-frequency bands does not alter the estimates of surface waves significantly.

Previous studies (Hasselmann et al. 1976; Mitsuyasu et al. 1980; Lewis and Allos 1990; Young 1998) report the values of nondimensional shape parameters σ_a, σ_b, and γ in the JONSWAP spectrum as varying within $\pm50\%$ of their mean values ($\sigma_a = 0.07$, $\sigma_b = 0.09$, and $\gamma = 3.3$). We estimate $\widetilde{f_p}^{\mathrm{ww3}}$ and $\widetilde{H_s}^{\mathrm{ww3}}$ using different values of σ_a, σ_b, and γ within $\pm50\%$ separately in the JONSWAP spectrum (Fig. 11) and conclude that the variations of the JONSWAP shape parameters within $\pm50\%$ have negligible effects on our surface wave estimates.

c. *Surface wave estimates from rotating-frame measurements*

Measurements of $\widetilde{\sigma_u}^2$ are affected by EM-APEX float rotation. The difference between $\widetilde{\sigma_u}^2$ and actual surface wave velocity variance depends on the float rotation rate and surface wave frequency, termed the rotational demodulation effect α in Eq. (5). Sanford et al. (2011) neglect the α effect and assume $\widetilde{\sigma_u}^2 = \sigma_{u0}^2\, e^{2kz}$ [i.e., $\alpha = 3$ in Eq. (5)], which may underestimate the $\sigma_{u0}^2\, e^{2kz}$ measured by the rotating electrodes. We use ww3 model simulations to quantify the α effect.

We simulate 2700 realizations of zonal propagating surface waves ($\theta = 0$) in each float profile using ww3 model outputs of S_η^{ww3}, assuming an initial phase ϕ_0 randomly distributed from 0 to 2π. The motional induction of simulated surface waves then generates the simulated electric current $\mathbf{J}'$ in the upper ocean [Eq. (3)]. The voltage measurements associated with simulated $\mathbf{J}'$ are taken by the electrodes at a constant rotation rate Ω [Eq. (B4)] and then processed to generate the simulations of estimated velocity variance $\widetilde{\sigma_{\mathrm{ww3}}}^2$ at the float positions [Eq. (5)]. The simulated rotation rate $\Omega/2\pi$ of electromagnetic (EM) sensors is varied from 0.05 to 0.25 Hz. The float vertical profiling speed is assumed to

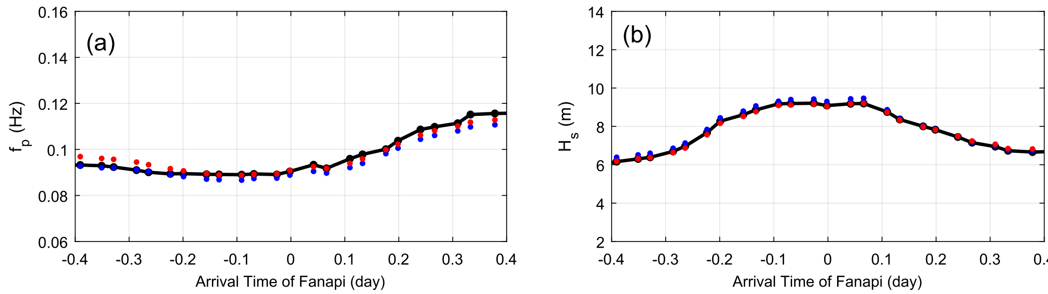

FIG. 10. (a) Peak frequency $\widetilde{f_p}^{\mathrm{ww3}}$ and (b) $\widetilde{H_s}^{\mathrm{ww3}}$ estimated using the ww3-simulated $\widetilde{\sigma_{\mathrm{ww3}}}^2$ at float em4907a, assuming the JONSWAP spectrum (blue dots) and the empirical spectrum in Donelan et al. (1985) (red dots). WAVEWATCH III model outputs are indicated (black lines).

be $0.11\,\mathrm{m\,s^{-1}}$, and the vertical resolution of $\widetilde{\sigma_{\mathrm{ww3}}}^2$ is ~3 m, similar to EM-APEX float measurements.

The $\widetilde{f_p}^{\mathrm{ww3}}$ and $\widetilde{H_s}^{\mathrm{ww3}}$ are estimated using the simulated float measurements $\widetilde{\sigma_{\mathrm{ww3}}}^2$ at float em4907a in the upper 100 m, assuming the JONSWAP spectrum [$\sigma_a = 0.07$, $\sigma_b = 0.09$, and $\gamma = 3.3$ in Eq. (D1)]. We compare the $\widetilde{f_p}^{\mathrm{ww3}}$ and $\widetilde{H_s}^{\mathrm{ww3}}$ with the actual ww3 model outputs of f_p^{ww3} and H_s^{ww3}. The $\widetilde{f_p}^{\mathrm{ww3}}$ is consistent with the f_p^{ww3}, and the standard deviation is <5% (Fig. 12a). The frequency difference between surface waves and rotating electrodes does not affect estimates of $\widetilde{f_p}^{\mathrm{ww3}}$. On the other hand, the $\widetilde{H_s}^{\mathrm{ww3}}$ is affected slightly by the difference between $\Omega/2\pi$ and $\widetilde{f_p}^{\mathrm{ww3}}$ (Fig. 12b). The $\widetilde{H_s}^{\mathrm{ww3}}/H_s^{\mathrm{ww3}}$ is about $1/\sqrt{2}$ if $|\widetilde{f_p} - \Omega/2\pi| > 0.07$ Hz and about 1/2 if $\widetilde{f_p} \approx \Omega/2\pi$. The amplitude of any signals measured by the rotating electrodes will remain at least $1/\sqrt{2}$ of their actual amplitude, that is, $\alpha = 1$ and $\widetilde{\sigma_u} = (1/\sqrt{2})\sigma_{u0}\, e^{kz}$ [Eq. (5)]. The smaller the difference between $\Omega/2\pi$ and $\widetilde{f_p}^{\mathrm{ww3}}$, the more measurements of surface wave velocity variance near the f_p with nonzero averages that are removed as the offset [Eq. (B5)]—that is, $\alpha \rightarrow 0$ and $\widetilde{\sigma_u} = (1/\sqrt{2})\sigma_{u0}\, e^{kz}$ [Eq. (5)]—and the $\widetilde{H_s}^{\mathrm{ww3}}$ underestimation increases.

The $\widetilde{H_s}^{\mathrm{ww3}}/H_s^{\mathrm{ww3}}$ is averaged within every ±0.01-Hz interval of $|\widetilde{f_p}^{\mathrm{ww3}} - (\Omega/2\pi)|$ to quantify the rotational demodulation effect α (Fig. 12b). The results at $|\widetilde{f_p}^{\mathrm{ww3}} - (\Omega/2\pi)| > 0.07$ Hz maintain the constant of $1/\sqrt{2}$. The float estimated $\widetilde{f_p}$ and the float rotation rate $\Omega/2\pi$ in this study are mostly within 0.04 Hz (covered by black bars in Fig. 12). The results averaged in $|\widetilde{f_p}^{\mathrm{ww3}} - (\Omega/2\pi)| = 0$–$0.04$ Hz are used to correct the float estimates of $\widetilde{H_s}$ (Fig. 4 in section 5), assuming surface waves with a random distribution of the initial phase.

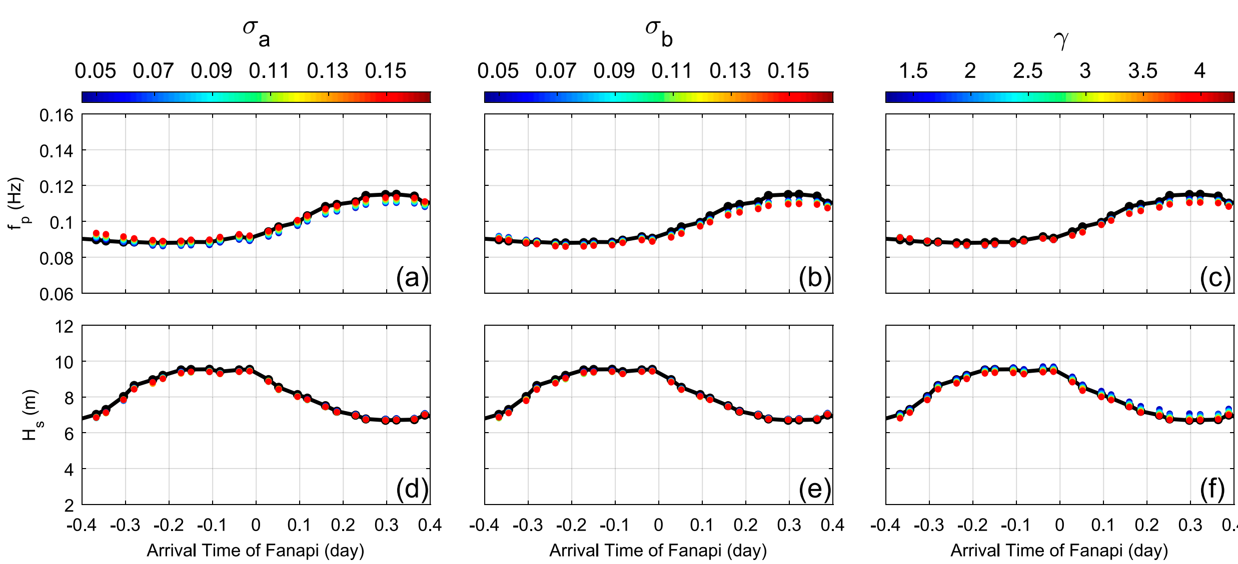

FIG. 11. (a)–(c) Peak frequency $\widetilde{f_p}^{\mathrm{ww3}}$ and (d)–(f) $\widetilde{H_s}^{\mathrm{ww3}}$ estimated using the ww3-simulated $\widetilde{\sigma_{\mathrm{ww3}}}^2$ at float em4907a, assuming different values for the shape parameters σ_a [different colored dots in (a) and (d) with $\gamma = 3.3$ and $\sigma_b = 0.09$], σ_b [different colored dots in (b) and (e) with $\gamma = 3.3$ and $\sigma_a = 0.07$], and γ [different colored dots in (c) and (f) with $\sigma_a = 0.07$ and $\sigma_b = 0.09$] in the JONSWAP spectrum. Actual ww3 model outputs (black lines with dots).

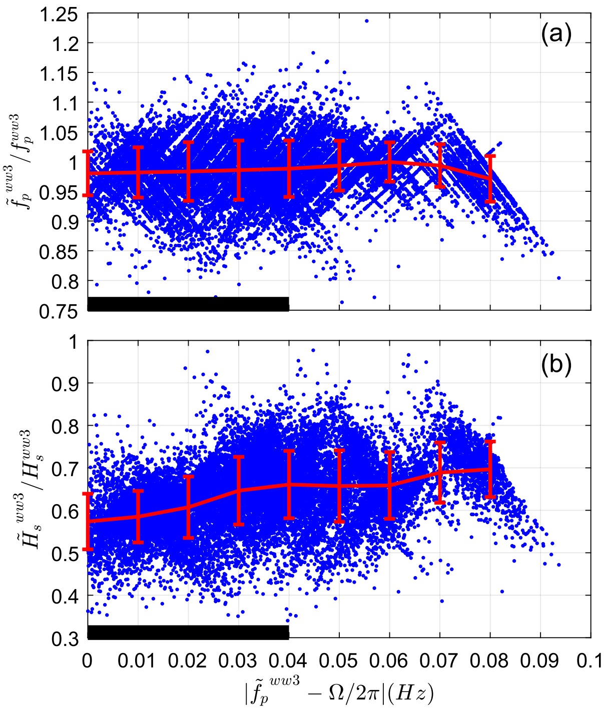

FIG. 12. Ratio of the ww3-estimated (a) $\widetilde{f_p}^{\text{ww3}}$ and (b) $\widetilde{H_s}^{\text{ww3}}$ to the actual ww3 model outputs of f_p^{ww3} and H_s^{ww3} at float em4907a. The mean and standard deviation are computed using the estimates in every ± 0.01 interval of $|\widetilde{f_p}^{\text{ww3}} - (\Omega/2\pi)|$ (red lines with vertical bars as one standard deviation), where Ω is the float angular rotation frequency. The range of $|\widetilde{f_p}^{\text{ww3}} - (\Omega/2\pi)|$ covering float estimates of surface waves in Fig. 4 is indicated (black bars).

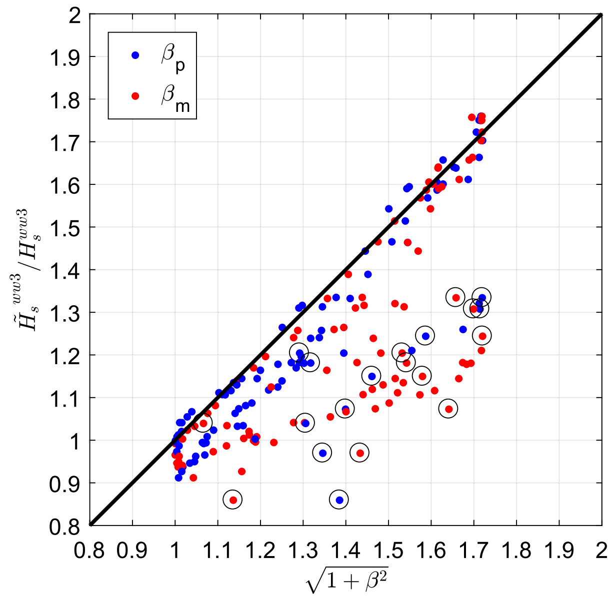

FIG. 13. Comparisons between the ratio of ww3-estimated $\widetilde{H_s}^{\text{ww3}}$ to actual ww3 model output of H_s^{ww3} and $\sqrt{1+\beta^2}$; $\widetilde{H_s}$ has already been corrected for the rotational demodulation effect α in Fig. 12b. The terms β_p and β_m are parameterized using the ww3 model outputs of surface wave direction at f_p (blue dots) and mean surface wave direction (red dots), respectively. Note that $\widetilde{H_s}^{\text{ww3}}$ for poor estimates of $(\widetilde{f_p}^{\text{ww3}} - f_p^{\text{ww3}})/f_p^{\text{ww3}} > 5\%$ (i.e., more than one standard deviation in Fig. 12a; circles). See Fig. 12 for the definitions of $\widetilde{f_p}^{\text{ww3}}$ and f_p^{ww3}. The term β_p is more suitable than β_m for correcting the uncertainties of $\widetilde{H_s}^{\text{ww3}}$ resulting from the geomagnetic field inclination effect.

d. Geomagnetic field inclination and surface wave propagation direction effects

Measurements of $\widetilde{\sigma_u}^2$ affected by the geomagnetic field inclination effect β ($=F_y/F_z \sin\theta$) are studied further [Eq. (5)]. The difference between $\widetilde{\sigma_u}^2$ and actual surface wave velocity variance depends on the geomagnetic field inclination F_y/F_z and surface wave propagation direction θ. Sanford et al. (2011) neglect the geomagnetic field's inclination effect [i.e., $\beta = 0$ in Eq. (5)], which may overestimate the surface wave velocity variance by more than 2 times for the meridional propagating surface waves ($\beta^2 = 2.25$) at the front-left quadrant of Fanapi (section 6).

We use the surface wave propagation direction θ from the ww3 model output [Eq. (4)] to assess the β effect on $\widetilde{H_s}^{\text{ww3}}$, because the β effect on $\widetilde{f_p}^{\text{ww3}}$ is negligible (not shown in this study). The $\widetilde{H_s}$ is estimated using 2700 realizations of simulated float measurements $\widetilde{\sigma_{\text{ww3}}}^2$ (section 7c) in the upper 100 m at float em4907a, assuming the JONSWAP spectrum [$\sigma_a = 0.07$, $\sigma_b = 0.09$, and $\gamma = 3.3$ in Eq. (D1)]. Estimates of $\widetilde{H_s}$ are averaged and corrected for the rotational demodulation effect α (Fig. 12b) using estimates of $\widetilde{f_p}^{\text{ww3}}$. We expect that, after averaging over a random initial phase, the ratio of corrected $\widetilde{H_s}^{\text{ww3}}$ to $\widetilde{H_s}^{\text{ww3}}$ equals $\sqrt{1+\beta^2}$ (Fig. 13), because $\widetilde{\sigma_u} \propto \sqrt{1+\beta^2}\sigma_{u0}$ [Eq. (5)].

The expression of β is for a single wave [Eq. (4)]. The effect of single wave-dependent β on $\widetilde{H_s}^{\text{ww3}}$ estimated assuming the JONSWAP spectrum also needs to be assessed. The parameters β_m and β_p are computed using the ww3 model outputs of mean surface wave direction and wave direction at peak frequency, respectively (Kuik et al. 1988). The correlation coefficient between $\widetilde{H_s}^{\text{ww3}}/H_s^{\text{ww3}}$ and $\sqrt{1+\beta_m^2}$ is about 0.75, and that between $\widetilde{H_s}^{\text{ww3}}/H_s^{\text{ww3}}$ and $\sqrt{1+\beta_p^2}$ is about 0.88 (Fig. 13). Estimates of $\widetilde{H_s}^{\text{ww3}}$ in this study are corrected for the β effect by dividing $\sqrt{1+\beta_p^2}$ by the $\widetilde{H_s}^{\text{ww3}}$ (Fig. 4 in section 5), that is, corrected $\widetilde{H_s}^{\text{ww3}} = \widetilde{H_s}^{\text{ww3}}/\sqrt{1+\beta_p^2}$. Most $\sqrt{1+\beta_p^2}$ outliers occur when the $(\widetilde{f_p}^{\text{ww3}} - f_p^{\text{ww3}})/f_p^{\text{ww3}}$ is more than 5% (more than one standard deviation in Fig. 12a), that is, when the estimates of $\widetilde{f_p}^{\text{ww3}}$ are poor. The root-mean-square (RMS) error between $\widetilde{H_s}^{\text{ww3}}/H_s^{\text{ww3}}$ and $\sqrt{1+\beta_p^2}$ is about 0.08 at $(\widetilde{f_p}^{\text{ww3}} - f_p^{\text{ww3}})/f_p^{\text{ww3}} < 5\%$. It is used as one standard deviation to run 1000 realizations of β_p as bootstrapping simulations to compute the uncertainties of corrected $\widetilde{H_s}^{\text{ww3}}$, ~8% (Fig. 4 in section 5).

8. Summary

Seven EM-APEX floats were air launched from a C-130 aircraft ahead of Typhoon Fanapi in 2010 (D'Asaro et al. 2014) to measure oceanic temperature, salinity, current velocity, and high-frequency velocity variance $\widetilde{\sigma_u}^2$ as the typhoon passed. The $\widetilde{\sigma_u}^2$ induced by the motion of surface waves (Longuet-Higgins et al. 1954; Sanford et al. 1978) in the upper 100 m are used to estimate the peak frequency $\widetilde{f_p}$ and the significant wave height $\widetilde{H_s}$, assuming the empirical JONSWAP spectrum under Typhoon Fanapi. The $\widetilde{f_p}$ and $\widetilde{H_s}$ are compared with the $\breve{f}_p$ and $\breve{H}_s$ estimated assuming a single dominant surface wave (Sanford et al. 2011), and the model outputs in the WAVEWATCH III model. The uncertainties of $\widetilde{f_p}$ and $\widetilde{H_s}$ on the EM-APEX floats as a result of assuming the JONSWAP spectrum are <5% outside Fanapi's eyewall, but sometimes they are >10% within the eyewall, which is assessed using the ww3 model outputs.

At 0.4 day before the arrival of Typhoon Fanapi's eye, the $\widetilde{f_p}$ is almost homogenous under Typhoon Fanapi, about 0.08 Hz. The $\widetilde{H_s}$ at the front-right quadrant of Typhoon Fanapi is about 6–10 m and can be 5 m higher than that on the front-left quadrant. The spatial variability of the surface wave height and wavelength before the arrival of Fanapi's eye has similar features to those reported using SRA measurements (Wright et al. 2001; Walsh et al. 2002; Fan et al. 2009). After the passage of Fanapi's eye, the $\widetilde{f_p}$ on the left-hand side of Fanapi's track changes more significantly than on the right-hand side of the track, from 0.08 to 0.1 Hz. The $\widetilde{H_s}$ can be >10 m at the rear-left quadrant of Typhoon Fanapi and is higher than those estimated using SRA measurements at the rear-left quadrant of hurricanes (e.g., Wright et al. 2001). The slow motion of Fanapi may reduce the extended fetch effect (Young 2003) at the rear sector of the storm.

Estimates of $\widetilde{f_p}$ and $\widetilde{H_s}$ are compared with $\breve{f}_p$ and $\breve{H}_s$, respectively. The $\widetilde{f_p}$ is mostly >0.01 Hz higher than $\breve{f}_p$ within 40 km of Fanapi's track at 0.2 day before the passage of Fanapi's eye. The greatest difference in peak frequency occurs on Fanapi's track, ~0.02 Hz. The difference between $\widetilde{H_s}$ and $\breve{H}_s$ is mostly 2–3 m, except for those estimates on the left-hand side of Fanapi's track. The difference in surface wave estimates is due to the surface wave spectrum assumed, that is, broad band versus narrow band. Assuming a broadband surface wave spectrum under tropical cyclones is more appropriate.

The $\widetilde{f_p}$ and $\widetilde{H_s}$ are also compared with the ww3 model outputs of f_p^{ww3} and H_s^{ww3}. The $\widetilde{f_p}$ is 10% lower than f_p^{ww3}, in good agreement with the ww3 validation by Fan et al. (2009). In the rear sector of Fanapi in the ww3 model, the $\widetilde{f_p}$ on the three EM-APEX floats within 40 km of Fanapi's track is at least 20% lower than the f_p^{ww3}. Differences between $\widetilde{H_s}$ and H_s^{ww3} are mostly within 2 m in the rear-right quadrant of Fanapi. In the rear-left quadrant of Fanapi, the $\widetilde{H_s}$ can be 5.5 m higher than the H_s^{ww3}.

This paper presents a method for using subsurface float measurements to study surface waves, avoiding the strong impacts of wave breaking and wind forcing on surface platforms. More than 180 surface wave estimates are presented at wind speeds > 20 m s^{-1} and outside of Fanapi's eyewall, including the complex surface wave field in the rear sector of storms (Black et al. 2007). In this study we use surface wave propagation direction θ from the ww3 model output to correct the β effect on $\widetilde{H_s}$. In future studies we will focus on developing a method to estimate θ using high-resolution voltage measurements. Direct observations of surface waves under tropical cyclones are crucial for guiding model simulations for studying typhoon wave–ocean interactions (Chen et al. 2013; Reichl et al. 2014).

Acknowledgments. The authors acknowledge the Office of Naval Research Physical Oceanography Program (N00014-08-1-0560, N00014-08-1-0577, N00014-10-1-0313, N00014-11-1-0375, N00014-14-1-0360) for their support; NOAA NCEP for providing the WAVEWATCH III model, version 5.16; and the 53rd Weather Reconnaissance Squadron for deploying the EM-APEX floats. The authors extend special thanks to J. Carlson and J. Dunlap for designing and building the EM sensor systems on the EM-APEX float and to one of the anonymous reviewers for providing useful comments to improve the manuscript.

APPENDIX A

Electric Current in the Motional Induction in the Upper Ocean

a. Electric current induced by a moving medium in Earth's geomagnetic field

Sanford (1971) describes the electric current in a moving medium as

$$\mathbf{J} = \sigma(\mathbf{E} + \mathbf{V} \times \mathbf{B}). \tag{A1}$$

The electric current $\mathbf{J}$ is driven by two voltage sources: $\mathbf{V} \times \mathbf{B}$ is the motional induction resulting from the ocean current (Longuet-Higgins et al. 1954) and the background electric field $\mathbf{E}$.

Based on the Maxwell–Faraday equation, $\mathbf{E}$ in a moving medium [Eq. (A1)] is the gradient of electrical potential Φ modulated by the temporal variation of the magnetic field ($\partial\mathbf{a}/\partial t$) in the ocean (Sanford 1971), that is,

$$\mathbf{E} = -\nabla\Phi - \frac{\partial \mathbf{a}}{\partial t}, \quad \text{(A2)}$$

where the gradient operator is $\nabla = \frac{\partial}{\partial x}\hat{\mathbf{i}} + \frac{\partial}{\partial y}\hat{\mathbf{j}} + \frac{\partial}{\partial z}\hat{\mathbf{k}}$.

Following Ampere's law (Sanford 1971; Podney 1975), the magnetic potential vector $\mathbf{a}$ is primarily associated with the electric current $\mathbf{J}$, assuming the aspect ratio of the ocean is $\ll O(1)$, that is,

$$\nabla \times (\nabla \times \mathbf{a}) \approx \mu \mathbf{J}. \quad \text{(A3)}$$

We assume the ambient magnetic field $\mathbf{B}$ in the ocean primarily consists of Earth's geomagnetic field ($\mathbf{F} = F_y\hat{\mathbf{j}} + F_z\hat{\mathbf{k}}$) and the electromagnetic field $\mathbf{b}$,

$$\mathbf{B} = \mathbf{F} + \mathbf{b}. \quad \text{(A4)}$$

The electromagnetic field $\mathbf{b}$ is the curl of $\mathbf{a}$, $\mathbf{b} = \nabla \times \mathbf{a}$.

Substituting Eqs. (A2)–(A4) into Eq. (A1), the electric current modulated by the electromagnetic field is

$$\frac{\mathbf{J}}{\sigma} = -\nabla\Phi + \mathbf{V} \times (\mathbf{F} + \mathbf{b}) - \frac{\partial \mathbf{a}}{\partial t}. \quad \text{(A5)}$$

Note that both $\mathbf{a}$ and $\mathbf{b}$ are functions of $\mathbf{J}$.

b. *Motional induction of surface waves in a moving medium*

In Eq. (A5), the $\mathbf{J}$ induced by surface waves is modulated by the temporal variation of magnetic vector potential $(\partial\mathbf{a}/_{\partial t})$ associated with the wave-induced electric current [Eq. (A3)] and the motional induction of surface waves in the electromagnetic field $\mathbf{V}_{\rm sgw} \times \mathbf{b}$, where $\mathbf{V}_{\rm sgw}$ is the velocity of surface waves in deep water. The $[-(\partial\mathbf{a}/_{\partial t}) + \mathbf{V}_{\rm sgw} \times \mathbf{b}] \ll (-\nabla\Phi + \mathbf{V}_{\rm sgw} \times \mathbf{F})$ will be shown in the following analysis, that is,

$$\frac{\mathbf{J}}{\sigma} \approx -\nabla\Phi + \mathbf{V}_{\rm sgw} \times \mathbf{F}. \quad \text{(A6)}$$

We perform the perturbation analysis of Eq. (A5) following Sanford (1971). The electric current induced by the motional induction of surface waves is the first-order term $\mathbf{J}^{(1)}$ (Longuet-Higgins et al. 1954), that is,

$$\frac{\mathbf{J}^{(1)}}{\sigma} = -\nabla\Phi + \mathbf{V}_{\rm sgw} \times \mathbf{F}. \quad \text{(A7)}$$

The higher-order electric current $\mathbf{J}^{(n)}$ is the sum of the first order of electric current $\mathbf{J}^{(1)}$ and the correction of electric current $\Delta\mathbf{J}^{(n)}$, that is,

$$\mathbf{J}^{(n)} = \mathbf{J}^{(1)} + \Delta\mathbf{J}^{(n)}; \quad \text{for} \quad n \ge 2.$$

The correction of electric current $\Delta\mathbf{J}^{(n+1)}$ caused by the electromagnetic field's temporal variation $\partial[\mathbf{a}^{(n+1)}]/\partial t$ and motional induction in $\mathbf{b}^{(n+1)}$ is associated with $\mathbf{J}^{(n)}$ following Ampere's law (Sanford 1971), that is,

$$\begin{aligned}\Delta\mathbf{J}^{(n+1)} &= \sigma\left\{-\frac{\partial[\mathbf{a}^{(n+1)}]}{\partial t} + \mathbf{V}_{\rm sgw} \times \mathbf{b}^{(n+1)}\right\}\\ &= \sigma\left\{-\frac{\partial}{\partial t}\iiint[\mu\mathbf{J}^{(n)}]\,dx\,dy\,dz + \mathbf{V}_{\rm sgw} \times \int(\mu\mathbf{J}^{(n)})\,dl\right\}; \quad \text{for} \quad n \ge 1,\end{aligned} \quad \text{(A8)}$$

where l is the length scale of surface waves over a surface wave period.

We assume that $\mathbf{a}^{(1)}$ and $\mathbf{b}^{(1)}$ are zero (Sanford 1971). The higher-order $\mathbf{a}^{(n+1)}$ and $\mathbf{b}^{(n+1)}$ are computed using $\mathbf{J}^{(n)}$ following Eq. (A8). The surface wave is assumed to propagate in the zonal direction to simplify the following scale analysis. Based on the linear wave theory, the horizontal and vertical scales of electric current induced by surface waves should be proportional to the inverse wavenumber k^{-1} of surface waves, and the temporal scale should be inversely proportional to the surface wave frequency ω. The magnitude of the corresponding correction on the second order of electric current $\Delta\mathbf{J}^{(2)}$ is

$$\begin{aligned}|\Delta\mathbf{J}^{(2)}| &= \sigma\left|-\frac{\partial\mathbf{a}^{(2)}}{\partial t} + \mathbf{V}_{\rm sgw} \times \mathbf{b}^{(2)}\right|\\ &= \sigma\left[-\frac{\partial}{\partial t}\left|\iiint(\mu\mathbf{J}^{(1)})\,dx\,dy\,dz\right| + \left|\mathbf{V}_{\rm sgw} \times \int\mu\mathbf{J}^{(1)}\,dl\right|\right] \approx m|\mathbf{J}^{(1)}|,\end{aligned}$$

where $m = \sigma\mu[-(\omega/k^2) + (A/k)]$ and A is the surface wave velocity amplitude. The scale of $|\Delta\mathbf{J}^{(n)}|$ can be expressed as

$$|\Delta\mathbf{J}^{(n)}| \approx |\mathbf{J}^{(1)}|\sum_{i=2}^{n} \mathrm{m}^{(i-1)} = |\mathbf{J}^{(1)}|\frac{m^n - m}{m-1}; \quad n \geq 2. \tag{A9}$$

The higher-order correction of electric current resulting from the time variation of the electromagnetic field $|\Delta\mathbf{J}^{(n)}|$ [Eq. (A9)] relative to the first-order electric current $|\mathbf{J}^{(1)}|$ [Eq. (A7)] is

$$\frac{|\Delta\mathbf{J}^{(n)}|}{|\mathbf{J}^{(1)}|} \approx \frac{|\mathbf{J}^{(1)}|\dfrac{m^n - m}{m-1}}{|\mathbf{J}^{(1)}|} = \frac{m^n - m}{m-1}; \quad n \geq 2.$$

The seawater's conductivity σ is $\sim$4 mho m^{-1} and $\mu \sim 4\pi \times 10^{-7}$ H m^{-1}. Under tropical cyclones the wave frequency $\omega/2\pi$ ~0.07–0.2 Hz (e.g., Collins et al. 2014), the wave height in deep water $\eta = (A/\omega)$ (Young 1998) is less than 20 m, and the wavelength ($\lambda = 2\pi/k$) ~100–300 m; that is, $\sigma\mu(\omega/k^2) \approx O(10^{-4})$, $\sigma\mu(\eta\omega/k) \ll O(10^{-3})$, and $|\Delta\mathbf{J}^{(n)}|/|\mathbf{J}^{(1)}| \ll 1$. The correction of the electromagnetic field induced by surface waves on the wave-induced electric current is negligible, as suggested by Weaver (1965) and Lilley et al. (2004); that is, the electric current induced by a single surface wave [Eq. (A7)] is in the same form as the electric current induced by a low-frequency current [Eq. (1)].

c. Electric current induced by a low-frequency current

Sanford et al. (1978) describe the electric current $\mathbf{J} = J_x\hat{\mathbf{i}} + J_y\hat{\mathbf{j}}$ induced by a low-frequency (<0.02 Hz) current $\mathbf{u} = u\hat{\mathbf{i}} + v\hat{\mathbf{j}}$ [Eq. (9) in Sanford et al. 1978], assuming the aspect ratio of oceanic current $\ll O(1)$ and excluding the effect of high-frequency surface waves, that is,

$$\begin{cases} \dfrac{J_x}{\sigma} = F_z v + \overline{\left(\dfrac{J_x}{\sigma}\right)}^{*} \\ \dfrac{J_y}{\sigma} = -F_z u + \overline{\left(\dfrac{J_y}{\sigma}\right)}^{*} \end{cases}, \tag{A10}$$

where $\overline{\left(\dfrac{J_x}{\sigma}\right)}^{*} = \overline{\left(\dfrac{J_x}{\sigma}\right)} - F_z\overline{v^*}$; $\overline{\left(\dfrac{J_y}{\sigma}\right)}^{*} = \overline{\left(\dfrac{J_y}{\sigma}\right)} + F_z\overline{u^*}$; $\overline{\mathbf{V}^*} = \overline{u^*}\hat{\mathbf{i}} + \overline{v^*}\hat{\mathbf{j}}$ is a depth-independent term, equivalent to $\nabla\Phi(-H)$ at the seafloor $-H$ (Sanford et al. 1978); and $\overline{\left(\dfrac{\mathbf{J}}{\sigma}\right)} = \overline{\left(\dfrac{J_x}{\sigma}\right)}\hat{\mathbf{i}} + \overline{\left(\dfrac{J_y}{\sigma}\right)}\hat{\mathbf{j}}$ represents all other depth-independent terms except $\overline{\mathbf{V}^*}$ (Sanford 1971), which is often assumed negligible compared to other terms (Sanford et al. 1978).

d. Electric current induced by a surface wave

In linear wave theory, the surface wave velocity $\mathbf{V}_{\mathrm{sgw}}$ in the deep ocean can be expressed (Young 1999) as follows:

$$\begin{aligned} \mathbf{V}_{\mathrm{sgw}} &= u_{\mathrm{sgw}}\hat{\mathbf{i}} + v_{\mathrm{sgw}}\hat{\mathbf{j}} + w_{\mathrm{sgw}}\hat{\mathbf{k}} \\ &= A(\sin\psi\cos\theta\hat{\mathbf{i}} + \sin\psi\sin\theta\hat{\mathbf{j}} - \cos\psi\hat{\mathbf{k}})\,e^{kz} \end{aligned} \tag{A11}$$

$$\psi = k_x x + k_y y - \omega t + \phi_0; \quad \theta = \tan^{-1}\frac{k_y}{k_x} \quad \text{and}$$

$$k = (k_x^2 + k_y^2)^{\frac{1}{2}},$$

where $A = \sigma_{u0}^2/2$ is the velocity amplitude of the surface wave at the ocean surface.

To derive the solution of electrical potential Φ induced by a surface wave, we first assume that the conductivity σ in the upper ocean is locally uniform, $\nabla(1/\sigma) = 0$, and the conservation of electric current $\mathbf{J}$, $\nabla\cdot\mathbf{J} = 0$ (Longuet-Higgins et al. 1954). The curl of Earth's geomagnetic field is $\nabla\times\mathbf{F} = 0$ in the upper ocean according to Maxwell's equations, because $\mathbf{F}$ originates in the core of Earth. Because the surface wave is irrotational ($\nabla\times\mathbf{V}_{\mathrm{sgw}} = 0$), the gradient of Eq. (1) in the upper ocean becomes

$$\begin{aligned} \nabla^2\Phi &= \nabla\cdot\left(\mathbf{V}_{\mathrm{sgw}}\times\mathbf{F} - \frac{\mathbf{J}}{\sigma}\right) = (\nabla\times\mathbf{V}_{\mathrm{sgw}})\cdot\mathbf{F} \\ &\quad - \mathbf{V}_{\mathrm{sgw}}\cdot(\nabla\times\mathbf{F}) - \nabla\left(\frac{\mathbf{J}}{\sigma}\right) = 0, \end{aligned} \tag{A12}$$

where the gradient operator $\nabla = (\partial/\partial x)\hat{\mathbf{i}} + (\partial/\partial y)\hat{\mathbf{j}} + (\partial/\partial z)\hat{\mathbf{k}}$. Surface waves decay exponentially with depth, so Φ generated by surface waves at $z = -\propto$ is assumed negligible. The general solution of Φ has the exponential form e^{kz}.

At the ocean surface, the component of electric current normal to the ocean surface is zero (Longuet-Higgins et al. 1954), that is,

$$\mathbf{J}\cdot\hat{\mathbf{n}} = 0 \quad \text{at} \quad z = \eta,$$

where $\hat{\mathbf{n}}$ is the unit vector normal to the ocean surface, and $z = \eta$ the ocean surface. The ratio of the wave height to wavelength is typically less than $O(0.1)$ (e.g., Wright et al. 2001; Hu and Chen 2011), or wave breaking will occur (Donelan et al. 2004). We assume $\hat{\mathbf{n}} \approx \hat{\mathbf{k}}$ and

$$J_z \approx 0 \quad \text{at} \quad z = 0.$$

The boundary condition at the sea surface can be assumed using the vertical components of Eq. (1) as follows:

$$\frac{\partial \Phi}{\partial z} \approx F_y u_{\mathrm{sgw}} \quad \text{at} \quad z = 0. \tag{A13}$$

Because a surface wave decays exponentially in depth, the induced Φ at $z = -\infty$ is assumed negligible, that is,

$$\Phi(z = -\infty) \approx 0. \tag{A14}$$

Using Eqs. (A11)–(A14), the Φ induced by a surface wave is

$$\Phi = \frac{1}{k} F_y (A \sin\psi \cos\theta \, e^{kz}) \tag{A15}$$

Substituting Eqs. (A11) and (A15) into Eq. (1), the components of electric current induced by a surface wave become

$$\begin{cases} \dfrac{J_x}{\sigma} = F_z v_{sgw} - F_y w_{sgw} - \dfrac{\partial \Phi}{\partial x} = A \sin\theta (F_z \sin\psi + F_y \cos\psi \sin\theta) \, e^{kz} & \text{(A16a)} \\ \dfrac{J_y}{\sigma} = -F_z u_{sgw} - \dfrac{\partial \Phi}{\partial y} = -A \cos\theta (F_z \sin\psi + F_y \cos\psi \sin\theta) \, e^{kz} \quad . & \text{(A16b)} \\ \dfrac{J_z}{\sigma} = F_y u_{sgw} - \dfrac{\partial \Phi}{\partial z} = 0 & \text{(A16c)} \end{cases}$$

The vertical electric current induced by the surface wave is zero. The equations given above can be simplified as follows:

$$\mathbf{J}/\sigma = \sqrt{2} \sigma_{u0} F_z \sqrt{1 + \beta^2} \sin\psi_\omega (\sin\theta \hat{\mathbf{i}} - \cos\theta \hat{\mathbf{j}}) \, e^{kz}, \tag{A17}$$

where $\psi_\omega = \psi + \tan^{-1}(\beta)$ and $\beta = (F_y/F_z) \sin\theta$.

APPENDIX B

Voltage Measurements and Data Processing on EM-APEX Floats

a. Voltage measurements on autonomous drifting floats

EM-APEX floats are designed to drift freely with the seawater horizontally. If the float velocity $\mathbf{V}_{\mathrm{EM}}$ is the same as seawater $\mathbf{V}$, then the electric field around the float ($-\nabla\Phi_{\mathrm{EM}}$) is (Sanford et al. 1978)

$$\nabla \Phi_{\mathrm{EM}} = (\mathbf{V}_{\mathrm{EM}} - \mathbf{V}) \times \mathbf{F} - \frac{\tilde{\mathbf{J}}}{\sigma} \approx -\frac{\tilde{\mathbf{J}}}{\sigma} \tag{B1}$$

$$\tilde{\mathbf{J}} = (1 + C_1)\mathbf{J}, \tag{B2}$$

where $\mathbf{J}$ is the electric current induced by the motion of seawater, and $\tilde{\mathbf{J}}$ is the electric current measured on the float, modified by the float's physical presence. The float's insulated outer surface stretches the path of electric current and its shape enhances the electrical potential density lead to a head factor C_1 (Sanford et al. 1978). The C_1 is ~0.5 for EM-APEX floats, as determined in the laboratory by comparing the voltage measurements in a water tank taken by EM-APEX floats and a T bar, which is a simple pair of electrodes. We assume its physical presence does not affect the electric current $\mathbf{J}$, that is, $C_1 = 0$ for T bar.

EM-APEX floats profile vertically at a vertical component of velocity w_{EM} relative to the surrounding water by adjusting the floats' buoyancy. The vertical motion generates a zonal component of electrical current, $F_y(1 + C_2)w_{\mathrm{EM}}\hat{\mathbf{i}}$, where the head factor C_2 is -0.2 (Sanford et al. 1978). Therefore, the electric field around the EM-APEX float is expressed as

$$\nabla \Phi_{\mathrm{EM}} \approx \left[F_y (1 + C_2) w_{\mathrm{EM}} - (1 + C_1) \frac{J_x}{\sigma} \right] \hat{\mathbf{i}} - (1 + C_1) \frac{J_y}{\sigma} \hat{\mathbf{j}}. \tag{B3}$$

b. Voltage measurements on the rotating electrodes

Two orthogonal pairs of Ag-AgCl electrodes, termed E_1 and E_2 pairs, are equipped on the EM-APEX floats to take voltage measurements (Fig. 2). Float voltage measurements $\Delta\Phi_i$ ($i = 1$ for the E_1 pair and $i = 2$ for the E_2 pair) primarily consist of the projections of the electric field on the electrodes [$-\nabla\Phi_{\mathrm{EM}}$, expressed in Eq. (B3)], a trend $\Delta\Phi_{\mathrm{trend}}$ resulting from the vertical variations of salinity and temperature, an unknown constant offset $\Delta\Phi_{\mathrm{offset}}$, and instrumental noise $\Delta\Phi_{\mathrm{noise}}$ (Sanford et al. 1978),

$$\begin{aligned} \frac{\Delta \Phi_i}{L} = & \left[F_y (1 + C_2) w_{\mathrm{EM}} - (1 + C_1) \left(\frac{J'_x}{\sigma} + \frac{\overline{J}_x}{\sigma} \right) \right] \cos\theta_\Omega \\ & - (1 + C_1) \left(\frac{J'_y}{\sigma} + \frac{\overline{J}_y}{\sigma} \right) \sin\theta_\Omega + \frac{\Delta \Phi_{\mathrm{trend}}}{L} t \\ & + \frac{\Delta \Phi_{\mathrm{offset}}}{L} + \frac{\Delta \Phi_{\mathrm{noise}}}{L}, \end{aligned} \tag{B4}$$

where L is the distance between electrodes, and the angle of the electrode pair from the geomagnetic east is $\theta_\Omega = \Omega t + \phi_i$. Note that $\overline{J_x}$ and $\overline{J_y}$ are electrical currents induced by the low-frequency current (< 0.02 Hz), and J'_x and J'_y are electrical currents induced by surface gravity waves (>0.02 Hz).

c. Voltage measurements associated with low-frequency electric currents

Low-frequency electric currents $\overline{\mathbf{J}}/\sigma$ taken by the EM-APEX floats are obtained by least squares fitting $\Delta\Phi_i$ [Eq. (B4)] in 50-s data windows, where the direction of EM sensors θ_Ω $(=\Omega t + \phi_i)$ is determined using the float's magnetometer measurements (e.g., Sanford et al. 1978, 2005), that is,

$$\frac{\Delta\Phi_i}{L} = \widetilde{a}_1 \cos\theta_\Omega + \widetilde{a}_2 \sin\theta_\Omega + \widetilde{a}_3 t + \widetilde{a}_4 + \varepsilon_i, \quad \text{for} \quad i = 1, 2 \tag{B5}$$

$$\begin{cases} \widetilde{a}_1 = -\dfrac{\overline{J_x}}{\sigma}(1 + C_1) + F_y(1 + C_2)w_{\mathrm{EM}} \\ \widetilde{a}_2 = -\dfrac{\overline{J_y}}{\sigma}(1 + C_1) \\ \widetilde{a}_3 = \dfrac{\Delta\Phi_{\mathrm{trend}}}{L} \\ \widetilde{a}_4 \approx -(1 + C_1)\langle\chi\rangle + \dfrac{\Delta\Phi_{\mathrm{offset}}}{L} \\ \varepsilon_i = -(1 + C_1)(\chi - \langle\chi\rangle) + \dfrac{\Delta\Phi_{\mathrm{noise}}}{L} \end{cases},$$

where $\widetilde{a}_1$–$\widetilde{a}_4$ are the fitting coefficients, ε_i is the residuals, $\chi = \frac{J'_x}{\sigma}\cos\theta_\Omega + \frac{J'_y}{\sigma}\sin\theta_\Omega$, and the angle brackets, $\langle\,\rangle$, represent the average over a 50-s fitting window. Note that because the surface wave period is typically much shorter than 50 s, only the electrical currents $\overline{J_x}$ and $\overline{J_y}$ induced by low-frequency oceanic currents are fitted in the 50-s data windows. The constant offset $\widetilde{a}_4$ may include the effects of surface waves if χ is not negligible (appendix B, section d).

d. Subsurface float measurements of velocity variance

The residuals ε_i [Eq. (B5)] associated with surface waves are used to compute the measured velocity variance $\widetilde{\sigma_u}^2$ as follows:

$$\widetilde{\sigma_u}^2 = \frac{\varepsilon_i^2}{(1 + C_1)^2 F_z^2} \approx \frac{\langle\chi^2\rangle - \langle\chi\rangle^2}{F_z^2} + \delta^2, \tag{B6}$$

where the angle brackets represent the average over a 50-s fitting window, the instrumental noise $\delta^2 = \left(\frac{\Delta\Phi_{\mathrm{noise}}}{L}\right)^2 / F_z^2(1 + C_1)^2$, and $\chi = (J'_x/\sigma)\cos\theta_\Omega + (J'_y/\sigma)\sin\theta_\Omega$. The term $\chi = (J'_x/\sigma)\cos\theta_\Omega + (J'_y/\sigma)\sin\theta_\Omega$ can be rewritten using Eq. (3) as follows:

$$\chi = \sqrt{2}\sigma_{u0}\sqrt{1 + \beta^2}F_z e^{kz} \sin\psi_\omega \sin\psi_\Omega, \tag{B7}$$

where $\theta_\Omega = \Omega t + \phi_i$ is the orientation of electrodes, and the angle difference between surface wave propagation direction and electrodes $\psi_\Omega = \theta - \theta_\Omega$. Because the surface wave period under tropical cyclones is usually <50 s (e.g., Collins et al. 2014), the averages of $\cos\psi_\omega$ and $\cos(\psi_\omega + \psi_\Omega)$ in the 50-s data window are

$$\langle\cos\psi_\omega\rangle = \langle\cos(\psi_\omega + \psi_\Omega)\rangle \approx 0. \tag{B8}$$

Substituting Eqs. (B7) and (B8) into the $\langle\chi^2\rangle$ and $\langle\chi\rangle^2$, respectively in Eq. (B6),

$$\begin{aligned} \frac{\langle\chi^2\rangle}{F_z^2(1 + \beta^2)\sigma_{u0}^2 e^{2kz}} &= 2\left\langle\sin^2\psi_\omega \sin^2\psi_\Omega\right\rangle \\ &= \frac{1}{2}\langle(1 - \cos2\psi_\omega)(1 - \cos2\psi_\Omega)\rangle \\ &\approx \frac{1}{2}\left[\frac{1}{2} + \langle\cos^2(\psi_\omega - \psi_\Omega)\rangle - \langle\cos2\psi_\Omega\rangle\right] \end{aligned}$$

$$\begin{aligned} \frac{\langle\chi\rangle^2}{F_z^2(1 + \beta^2)\sigma_{u0}^2 e^{2kz}} &= 2\left\langle\sin\psi_\omega \sin\psi_\Omega\right\rangle^2 \\ &= \frac{1}{2}\langle\cos(\psi_\omega - \psi_\Omega) - \cos(\psi_\omega + \psi_\Omega)\rangle^2 \\ &\approx \frac{1}{2}\langle\cos(\psi_\omega - \psi_\Omega)\rangle^2 \end{aligned}$$

the $\widetilde{\sigma_u}^2$ becomes

$$\widetilde{\sigma_u}^2 \approx \frac{\sigma_{u0}^2}{2}\left[\frac{1}{2} + \langle\cos^2(\psi_\omega - \psi_\Omega)\rangle - \langle\cos(\psi_\omega - \psi_\Omega)\rangle^2 - \langle\cos2\psi_\Omega\rangle\right](1 + \beta^2)e^{2kz} + \delta^2. \tag{B9}$$

The estimated velocity variance $\widetilde{\sigma_u}^2$ in Eq. (B9) can be rewritten as

$$\widetilde{\sigma_u}^2 \approx \frac{(1 + \alpha)}{4}(1 + \beta^2)\sigma_{u0}^2 e^{2kz} + \delta^2, \tag{B10}$$

where $\alpha = 2\langle\cos^2\tilde{\psi}\rangle - 2\langle\cos\tilde{\psi}\rangle^2 - 2\langle\cos2\psi_\Omega\rangle$ is termed the rotational demodulation effect in this study, $\tilde{\psi} = -(\omega - \Omega)t + \widetilde{\phi_0}$ is the difference between the surface wave angular frequency ω and the float angular rotation frequency Ω, and $\widetilde{\phi_0} = k_x x + k_y y + \phi_0 + \phi_i + \tan^{-1}(\beta) - \theta$.

APPENDIX C

Profiles of Surface Wave Horizontal Velocity Variance σ_u^2

According to the linear wave theory of surface waves in the deep ocean (Young 1999), the velocity of surface waves decays exponentially at the rate of k^{-1} in depth, where k is the wavenumber, and the ratio of surface wave horizontal velocity to ocean surface displacement η equals the angular frequency $\omega = 2\pi f$. We can relate the horizontal velocity spectrum S_u and the ocean surface displacement spectrum S_η as (Young 1999)

$$S_u(f, z) = \omega^2 S_\eta(f)\, e^{2kz}. \tag{C1}$$

The dispersion relationship of surface waves in the deep ocean is $\omega^2 = gk$. Integrating the surface wave velocity spectrum S_u [Eq. (C1)] at different depths, the profiles of surface wave horizontal velocity variance σ_u^2 can be computed as

$$\sigma_u^2(S_\eta, z) = \int S_u(f, z)\, df = \int \left[\omega^2 S_\eta(f)\, e^{\frac{2\omega^2 z}{g}}\right] df. \tag{C2}$$

The σ_u^2 in the deep ocean can be computed using $S_\eta(f)$, which will be implemented by the empirical surface wave spectrum reported in previous studies (appendix D). Note that the variance of ocean surface displacement $\sigma_\eta^2 (= \int S_\eta\, df)$ resulting from surface waves is proportional to the surface wave horizontal velocity variance $\sigma_u^2 (= \int S_u\, df)$.

APPENDIX D

Empirical Surface Wave Model Spectrum

a. *JONSWAP surface wave spectrum*

The Joint North Sea Wave Project (JONSWAP) conducted a series of experiments in the 1960s to study the surface wave field in the North Atlantic Ocean (Hasselmann et al. 1973). An empirical surface wave spectrum, often termed the JONSWAP spectrum, is expressed as

$$S_\eta = S_p \left(\frac{f}{f_p}\right)^{-5} \exp\left\{-\frac{5}{4}\left[\left(\frac{\mathrm{f}}{\mathrm{f_p}}\right)^{-4} - 1\right]\right\} \gamma^{\exp\left[-\frac{(f-f_p)^2}{2\sigma^2 f_p^2}\right] - 1}$$
$$\begin{cases} \sigma = \sigma_a & \text{at} \quad f \le f_p \\ \sigma = \sigma_b & \text{at} \quad f > f_p \end{cases}, \tag{D1}$$

where the peak enhancement factor γ equals 1 when surface waves reach their full development (Pierson and Moskowitz 1964). The parameters σ_a and σ_b define the width of the spectral peak region (Young 1999). Note that the JONSWAP spectrum is a monomodal frequency spectrum, which concentrates energy within a narrow frequency band. The mean values of σ_a, σ_b, and γ reported by Hasselmann et al. (1973) are 0.07, 0.09, and 3.3, respectively. The JONSWAP spectrum is first used for least squares fitting the velocity variance measured by EM-APEX floats in this study.

b. *Surface wave spectrum in Donelan et al. (1985)*

Donelan et al. (1985) studied the surface wave spectra in Lake Ontario in different sea states, $\upsilon = f_p|\mathbf{U}_{10}|/g$. The empirical surface wave spectrum form is expressed as

$$S_\eta = S_p \left(\frac{f}{f_p}\right)^{-4} \exp\left\{-\left[\left(\frac{f}{f_p}\right)^{-4} - 1\right]\right\} \gamma_d^{\exp\left[-\frac{(f-f_p)^2}{2\sigma_d^2 f_p^2}\right] - 1} \tag{D2}$$
$$\gamma_d = \begin{cases} 6.489 + 6\log(\upsilon); & \text{if} \quad \upsilon \ge 0.159 \\ 1.7; & \text{if} \quad \upsilon < 0.159 \end{cases}$$
$$\sigma_d = 0.08 + 1.29 \times 10^{-3} \upsilon^{-3},$$

where γ_d is the peak enhancement factor in the Donelan spectrum, $|\mathbf{U}_{10}|$ is Fanapi's wind speed at 10-m height above the sea surface (appendix E), and the parameter σ_d defines the width of the spectral peak region. The high-frequency portion of the Donelan spectrum decays in f^{-4}, whereas the JONSWAP spectrum decays in f^{-5} [Eq. (D1)].

APPENDIX E

Typhoon Fanapi's Wind Field

The ITOP project is an international joint field experiment conducted in the western Pacific in 2010 to study the oceanic response under three tropical cyclones: Fanapi, Malakas, and Megi (D'Asaro et al. 2014). About 139 dropsondes were deployed from a C-130 aircraft to measure the vertical wind profiles in Typhoon Fanapi during 14–18 September, with complementary measurements of wind speed at 10-m height above the sea surface taken by a Stepped Frequency Microwave Radiometer (SFMR) mounted on the C-130 aircraft. With data assimilation of dropsondes and SFMR wind measurements, the wind field under Typhoon Fanapi is modeled using the Weather Research and Forecasting (WRF) Model, supplemented with Navy Operational Global Atmospheric Prediction System (NOGAPS) products (Ko et al. 2014). The temporal resolution is 1 h, and the horizontal spatial resolution is 0.0375° latitude × 0.0375° longitude. At 0130 UTC 18 September

2010, the maximum wind radius of Typhoon Fanapi was about 30 km, the maximum wind speed about 43 m s^{-1}, and the translation speed about 4 m s^{-1} (Fig. 1).

REFERENCES

Black, P. G., and Coauthors, 2007: Air–sea exchange in hurricanes: Synthesis of observations from the Coupled Boundary Layer Air–Sea Transfer experiment. *Bull. Amer. Meteor. Soc.*, **88**, 357–374, https://doi.org/10.1175/BAMS-88-3-357.

Chen, S. S., W. Zhao, M. A. Donelan, and H. L. Tolman, 2013: Directional wind–wave coupling in fully coupled atmosphere–wave–ocean models: Results from CBLAST-Hurricane. *J. Atmos. Sci.*, **70**, 3198–3215, https://doi.org/10.1175/JAS-D-12-0157.1.

Collins, C. O., III, 2014: Typhoon generated surface gravity waves measured by NOMAD-type buoys. Ph.D. dissertation, University of Miami, 318 pp.

——, B. Lund, R. J. Ramos, W. M. Drennan, and H. C. Graber, 2014: Wave measurement intercomparison and platform evaluation during the ITOP (2010) experiment.*J. Atmos. Oceanic Technol.*, **31**, 2309–2329, https://doi.org/10.1175/JTECH-D-13-00149.1.

Cox, C., N. Kroll, P. Pistek, and K. Watson, 1978: Electromagnetic fluctuations induced by wind waves on the deep-sea floor. *J. Geophys. Res.*, **83**, 431–442, https://doi.org/10.1029/JC083iC01p00431.

D'Asaro, E. A., and Coauthors, 2014: Impact of typhoons on the ocean in the Pacific. *Bull. Amer. Meteor. Soc.*, **95**, 1405–1418, https://doi.org/10.1175/BAMS-D-12-00104.1.

Dietrich, J. C., and Coauthors, 2011: Hurricane Gustav (2008) waves and storm surge: Hindcast, synoptic analysis, and validation in southern Louisiana. *Mon. Wea. Rev.*, **139**, 2488–2522, https://doi.org/10.1175/2011MWR3611.1.

Donelan, M. A., J. Hamilton, and W. H. Hui, 1985: Directional spectra of wind-generated waves. *Philos. Trans. Roy. Soc. London*, **315A**, 509–562, https://doi.org/10.1098/rsta.1985.0054.

——, B. K. Haus, N. Reul, W. J. Plant, M. Stiassnie, H. C. Graber, O. B. Brown, and E. S. Saltzman, 2004: On the limiting aerodynamic roughness of the ocean in very strong winds. *Geophys. Res. Lett.*, **31**, L18306, https://doi.org/10.1029/2004GL019460.

Drennan, W. M., H. C. Graber, C. O. Collins III, A. Herrera, H. Potter, R. J. Ramos, and N. J. Williams, 2014: EASI: An air–sea interaction buoy for high winds. *J. Atmos. Oceanic Technol.*, **31**, 1397–1409, https://doi.org/10.1175/JTECH-D-13-00201.1.

Emanuel, K. A., 1995: Sensitivity of tropical cyclones to surface exchange coefficients and a revised steady-state model incorporating eye dynamics. *J. Atmos. Sci.*, **52**, 3969–3976, https://doi.org/10.1175/1520-0469(1995)052<3969:SOTCTS>2.0.CO;2.

Fan, Y., and W. E. Rogers, 2016: Drag coefficient comparisons between observed and model simulated directional wave spectra under hurricane conditions. *Ocean Modell.*, **102**, 1–13, https://doi.org/10.1016/j.ocemod.2016.04.004.

——, I. Ginis, T. Hara, C. W. Wright, and E. J. Walsh, 2009: Numerical simulations and observations of surface wave fields under an extreme tropical cyclone. *J. Phys. Oceanogr.*, **39**, 2097–2116, https://doi.org/10.1175/2009JPO4224.1.

Graber, H. C., E. A. Terray, M. A. Donelan, W. M. Drennan, J. C. V. Leer, and D. B. Peters, 2000: ASIS—A new air–sea interaction spar buoy: Design and performance at sea. *J. Atmos. Oceanic Technol.*, **17**, 708–720, https://doi.org/10.1175/1520-0426(2000)017<0708:AANASI>2.0.CO;2.

Hasselmann, K., and Coauthors, 1973: Measurements of wind-wave growth and swell decay during the Joint North Sea Wave Project (JONSWAP). Ergnzungsheft zur Deutschen Hydrographischen Zeitschrift Reihe A 8-12, Deutsches Hydrographisches Institute, 95 pp.

——, W. Sell, D. B. Ross, and P. Müller, 1976: A parametric wave prediction model. *J. Phys. Oceanogr.*, **6**, 200–228, https://doi.org/10.1175/1520-0485(1976)006<0200:APWPM>2.0.CO;2.

Hasselmann, S., K. Hasselmann, J. H. Allender, and T. P. Barnett, 1985: Computations and parameterizations of the nonlinear energy transfer in a gravity-wave spectrum. Part II: Parameterizations of the nonlinear energy transfer for application in wave models. *J. Phys. Oceanogr.*, **15**, 1378–1391, https://doi.org/10.1175/1520-0485(1985)015<1378:CAPOTN>2.0.CO;2.

Herbers, T. H. C., P. F. Jessen, T. T. Janssen, D. B. Colbert, and J. H. MacMahan, 2012: Observing ocean surface waves with GPS-tracked buoys. *J. Atmos. Oceanic Technol.*, **29**, 944–959, https://doi.org/10.1175/JTECH-D-11-00128.1.

Holthuijsen, L. H., M. D. Powell, and J. D. Pietrzak, 2012: Wind and waves in extreme hurricanes. *J. Geophys. Res.*, **117**, C09003, https://doi.org/10.1029/2012JC007983.

Hsu, J.-Y., R.-C. Lien, E. D'Asaro, and T. B. Sanford, 2017: Estimates of surface wind stress and drag coefficients in Typhoon Megi 2010. *J. Phys. Oceanogr.*, **47**, 545–565, https://doi.org/10.1175/JPO-D-16-0069.1.

Hu, K., and Q. Chen, 2011: Directional spectra of hurricane-generated waves in the Gulf of Mexico. *Geophys. Res. Lett.*, **38**, L19608, https://doi.org/10.1029/2011GL049145.

Hwang, P. A., D. W. Wang, E. J. Walsh, W. B. Krabill, and R. N. Swift, 2000: Airborne measurements of the wavenumber spectra of ocean surface waves. Part I: Spectral slope and dimensionless spectral coefficient. *J. Phys. Oceanogr.*, **30**, 2753–2767, https://doi.org/10.1175/1520-0485(2001)031<2753:AMOTWS>2.0.CO;2.

Jan, S., Y. J. Yang, H.-I. Chang, M.-H. Chang, and C.-L. Wei, 2017: New data buoys watch typhoons from within the storm. *Eos, Trans. Amer. Geophys. Union*, **98**, https://doi.org/10.1029/2017EO069821.

Ko, D. S., S.-Y. Chao, C.-C. Wu, and I. I. Lin, 2014: Impacts of Typhoon Megi (2010) on the South China Sea. *J. Geophys. Res. Oceans*, **119**, 4474–4489, https://doi.org/10.1002/2013JC009785.

Kuik, A. J., G. P. V. Vledder, and L. H. Holthuijsen, 1988: A method for the routine analysis of pitch-and-roll buoy wave data. *J. Phys. Oceanogr.*, **18**, 1020–1034, https://doi.org/10.1175/1520-0485(1988)018<1020:AMFTRA>2.0.CO;2.

Lewis, A. W., and R. N. Allos, 1990: JONSWAP's parameters: Sorting out the inconsistencies. *Ocean Eng.*, **17**, 409–415, https://doi.org/10.1016/0029-8018(90)90032-2.

Lilley, F. E. M., A. P. Hitchman, P. R. Milligan, and T. Pedersen, 2004: Sea-surface observations of the magnetic signals of ocean swells. *Geophys. J. Int.*, **159**, 565–572, https://doi.org/10.1111/j.1365-246X.2004.02420.x.

Lin, I.-I., and Coauthors, 2013: An ocean coupling potential intensity index for tropical cyclones. *Geophys. Res. Lett.*, **40**, 1878–1882, https://doi.org/10.1002/grl.50091.

Lin, W., L. P. Sanford, and S. E. Suttles, 2002: Wave measurement and modeling in Chesapeake Bay. *Cont. Shelf Res.*, **22**, 2673–2686, https://doi.org/10.1016/S0278-4343(02)00120-6.

Longuet-Higgins, M. S., M. E. Stern, and H. Stommel, 1954: The electrical field induced by ocean currents and waves, with applications to the method of towed electrode. *Pap. Phys. Oceanogr. Meteor.*, **13** (1), 1–37, https://doi.org/10.1575/1912/1064.

Magnusson, A. K., and Donelan, M. A., 2013: The Andrea wave characteristics of a measured North Sea rogue wave. *J. Offshore Mech. Arctic Eng.*, **135**, 031108, https://doi.org/10.1115/1.4023800.

Mitsuyasu, H., F. Tasai, T. Suhara, S. Mizuno, M. Ohkusu, T. Honda, and K. Rikiishi, 1975: Observations of the directional spectrum of ocean waves using a cloverleaf buoy. *J. Phys. Oceanogr.*, **5**, 750–760, https://doi.org/10.1175/1520-0485(1975)005<0750:OOTDSO>2.0.CO;2.

——, ——, ——, ——, ——, ——, and ——, 1980: Observation of the power spectrum of ocean waves using a cloverleaf buoy. *J. Phys. Oceanogr.*, **10**, 286–296, https://doi.org/10.1175/1520-0485(1980)010<0286:OOTPSO>2.0.CO;2.

Moon, I.-J., I. Ginis, and T. Hara, 2004: Effect of surface waves on air–sea momentum exchange. Part II: Behavior of drag coefficient under tropical cyclones. *J. Atmos. Sci.*, **61**, 2334–2348, https://doi.org/10.1175/1520-0469(2004)061<2334:EOSWOA>2.0.CO;2.

Mrvaljevic, R. K., and Coauthors, 2013: Observations of the cold wake of Typhoon Fanapi (2010). *Geophys. Res. Lett.*, **40**, 316–321, https://doi.org/10.1029/2012GL054282.

Ochi, M. K., Ed., 2003: *Hurricane-Generated Seas*. Elsevier Ocean Engineering Series, Vol. 8, Elsevier, 140 pp., https://doi.org/10.1016/s1571-9952(03)x8018-6.

——, and Chiu, M.-H., 1982: Nearshore wave spectra measured during Hurricane David. *Coastal Engineering 1982: Proceedings of the Eighteen Coastal Engineering Conference*, B. L. Edge, Ed., Vol. 1, ASCE, 77–86, https://doi.org/10.1061/9780872623736.005.

Pierson, W. J., and L. Moskowitz, 1964: A proposed spectral form for fully developed wind seas based on the similarity theory of S. A. Kitaigorodskii. *J. Geophys. Res.*, **69**, 5181–5190, https://doi.org/10.1029/JZ069i024p05181.

Pinkel, R., and J. A. Smith, 1987: Open ocean surface wave measurement using Doppler sonar. *J. Geophys. Res.*, **92**, 12 967–12 973, https://doi.org/10.1029/JC092iC12p12967.

Podney, W., 1975: Electromagnetic fields generated by ocean waves. *J. Geophys. Res.*, **80**, 2977–2990, https://doi.org/10.1029/JC080i021p02977.

Potter, H., C. O. Collins III, W. M. Drennan, and H. C. Graber, 2015: Observations of wind stress direction during Typhoon Chaba (2010). *Geophys. Res. Lett.*, **42**, 9898–9905, https://doi.org/10.1002/2015GL065173.

Price, J. F., T. B. Sanford, and G. Z. Forristall, 1994: Forced stage response to a moving hurricane. *J. Phys. Oceanogr.*, **24**, 233–260, https://doi.org/10.1175/1520-0485(1994)024<0233:FSRTAM>2.0.CO;2.

Reichert, K., K. Hessner, J. C. Nieto Borge, and J. Dittmer, 1999: WaMoS II: A radar based wave and current monitoring system. *Proceedings of the Ninth (1999) International Offshore and Polar Engineering Conference*, J. S. Chung, T. Matsui, and W. Koterayama, Eds., Vol. 3, ISOPE, 139–143.

Reichl, B. G., T. Hara, and I. Ginis, 2014: Sea state dependence of the wind stress over the ocean under hurricane winds. *J. Geophys. Res. Oceans*, **119**, 30–51, https://doi.org/10.1002/2013JC009289.

Roy, T., 1994: Bootstrap accuracy for non-linear regression models. *J. Chemom.*, **8**, 37–44, https://doi.org/10.1002/cem.1180080105.

Sanford, T. B., 1971: Motionally induced electric and magnetic fields in the sea. *J. Geophys. Res.*, **76**, 3476–3492, https://doi.org/10.1029/JC076i015p03476.

——, R. G. Drever, and J. H. Dunlap, 1978: A velocity profiler based on the principles of geomagnetic induction. *Deep-Sea Res.*, **25**, 183–210, https://doi.org/10.1016/0146-6291(78)90006-1.

——, J. H. Dunlap, J. A. Carlson, D. C. Webb, and J. B. Girton, 2005: Autonomous velocity and density profiler: EM-APEX. *Proceedings of the IEEE/OES Eighth Working Conference on Current Measurement Technology, 2005*, IEEE, 152–156, https://doi.org/10.1109/CCM.2005.1506361.

——, J. F. Price, and J. B. Girton, 2011: Upper-ocean response to Hurricane Frances (2004) observed by profiling EM-APEX floats. *J. Phys. Oceanogr.*, **41**, 1041–1056, https://doi.org/10.1175/2010JPO4313.1.

Steele, K. E., C.-C. Teng, and D. W. C. Wang, 1992: Wave direction measurements using pitch-roll buoys. *Ocean Eng.*, **19**, 349–375, https://doi.org/10.1016/0029-8018(92)90035-3.

Thébault, E., and Coauthors, 2015: International geomagnetic reference field: The 12th generation. *Earth Planets Space*, **67**, 79, https://doi.org/10.1186/s40623-015-0228-9.

Tolman, H. L., and D. Chalikov, 1996: Source terms in a third-generation wind wave model. *J. Phys. Oceanogr.*, **26**, 2497–2518, https://doi.org/10.1175/1520-0485(1996)026<2497:STIATG>2.0.CO;2.

Walsh, E. J., and Coauthors, 2002: Hurricane directional wave spectrum spatial variation at landfall. *J. Phys. Oceanogr.*, **32**, 1667–1684, https://doi.org/10.1175/1520-0485(2002)032<1667:HDWSSV>2.0.CO;2.

Watermann, J., and A. Magunia, 1997: Propagation parameters of sea surface waves inferred from observations from two closely spaced vector magnetometers. *J. Geomagn. Geoelectr.*, **49**, 709–720, https://doi.org/10.5636/jgg.49.709.

WAVEWATCH III Development Group, 2016: User manual and system documentation of WAVEWATCH III version 5.16. NOAA/NWS/NCEP/MMAB Tech. Note 329, 326 pp. + appendices.

Weaver, J. T., 1965: Magnetic variations associated with ocean waves and swell. *J. Geophys. Res.*, **70**, 1921–1929, https://doi.org/10.1029/JZ070i008p01921.

Wright, C. W., and Coauthors, 2001: Hurricane directional wave spectrum spatial variation in the open ocean. *J. Phys. Oceanogr.*, **31**, 2472–2488, https://doi.org/10.1175/1520-0485(2001)031<2472:HDWSSV>2.0.CO;2.

Young, I. R., 1998: Observations of the spectra of hurricane generated waves. *Ocean Eng.*, **25**, 261–276, https://doi.org/10.1016/S0029-8018(97)00011-5.

——, 1999: *Wind Generated Ocean Waves*. Elsevier Ocean Engineering Series, Vol. 2, Elsevier, 288 pp., https://doi.org/10.1016/s1571-9952(99)x8001-9.

——, 2003: A review of the sea state generated by hurricanes. *Mar. Struct.*, **16**, 201–218, https://doi.org/10.1016/S0951-8339(02)00054-0.

——, 2006: Directional spectra of hurricane wind waves. *J. Geophys. Res.*, **111**, C08020, https://doi.org/10.1029/2006jc003540.

——, and G. P. Burchell, 1996: Hurricane generated waves as observed by satellite. *Ocean Eng.*, **23**, 761–776, https://doi.org/10.1016/0029-8018(96)00001-7.

——, and J. Vinoth, 2013: An ''extended fetch'' model for the spatial distribution of tropical cyclone wind–waves as observed by altimeter. *Ocean Eng.*, **70**, 14–24, https://doi.org/10.1016/j.oceaneng.2013.05.015.